MULTI-OBJECTIVE OPTIMIZATION OF A LATTICE STRUCTURE—APPLICATION TO THE DESIGN OF A PEDESTRIAN BRIDGE

Angela Badrieh

Department of Mechanical Engineering

McGill University, Montréal

August 2014

A Thesis submitted to the Faculty of Graduate Studies and Research

in partial fulfilment of the requirements for the degree of

Master's Thesis Program

ABSTRACT

This research work targets the design and optimization of a bio-inspired pedestrian bridge. The bridge is made of lattice material, whose stress analysis is conducted by means of the theory of asymptotic homogenization, coupled with an optimization process that tailors the material properties to meet the functional requirements of the bridge. The analysis requires decoupling the system into two levels, system and component; the former represents the whole superstructure, the latter the cross-section of the bridge. The optimum solution describing the material properties of the bridge mapped into a lattice geometry, which enables the fabrication of the structure using additive manufacturing.

RÉSUMÉ

Ce travail de recherche a pour objectif la conception et l'optimisation d'un pont à piétons bio-inspiré. Le pont est constitué de matériel réseau dont l'analyse est faite à l'aide de la théorie de l'homogénéisation asymptotique, couplée avec un processus d'optimisation qui adapte les propriétés mécaniques afin d'atteindre les exigences fonctionnelles du pont. L'analyse nécessite la division du système en deux niveaux, système et composant; le précédent représente la superstructure en entière, le dernier la section transversale du pont. La solution optimale décrivant les propriétés du pont peut être traduite en géométrie en réseau, ce qui permet la construction de la structure en utilisant la fabrication additive.

ACKNOWLEDGMENTS

I would like to express my appreciation to my supervisors, Professor Jorge Angeles, Professor Damiano Pasini and Professor Aaron Sprecher for their continuous support throughout all my research at McGill. I would also like to thank all my colleagues from the three different labs for their tremendous help, especially Hang Xu, Purnendu Prithipaul, Vikram Chopra and François Le Blanc. Finally, I want to address special thanks for my family and friends who never stopped supporting me even from miles away, and to the dear friends I met along the way.

TABLE OF CONTENTS

LIST OF FIGURES

CHAPTER 1

Introduction

The research work reported here is established by the fusion of many disciplines. From biomimetics and architecture, through functionally graded materials and cellular materials, to civil engineering, optimization and fabrication, a wide range of fields is integrated into a novel design paradigm. This is then applied to the design of a pedestrian bridge. Therefore, the bridge thus designed is a nature-inspired optimum structure, made of innovative materials and fabricated with innovative technologies.

Following the model proposed by French for the design process, as shown in Fig. 1.1 (French, 1999), the first stage of the process is the need that gave rise to the design task. For this specific design task, we can depart from the configuration of conventional bridges, such as the Charlevoix bridge over Lachine Canal in Montreal, as shown in Fig. 1.2. These bridges require regular maintenance as they are made of traditional materials, such as steel, susceptible of corrosion, with standard bridge models such as truss bridges. A few Montreal bridges visited when planning this work provide very narrow and exposed routes for pedestrians, which become dangerous under severe weather conditions. Additionally safe pedestrian passages across the path of trains are generally lacking. As such, there is a need for safe and comfortable

pedestrian bridges ensuring protection for people from the elements, while guaranteeing conformity with the surrounding environment. The first stage is the analysis of the problem, an activity, according to the French model, concerning the development of a design that satisfies the described needs. Such a design would address the problems faced with conventional bridges, especially in terms of the environmental impact of the structure, in addition to the optimization of structural and material properties leading to the enhancement of cost and structural efficiency of the bridge. This is to be constructed with innovative manufacturing processes that can be more user-friendly and effective with respect to the model of the structure.

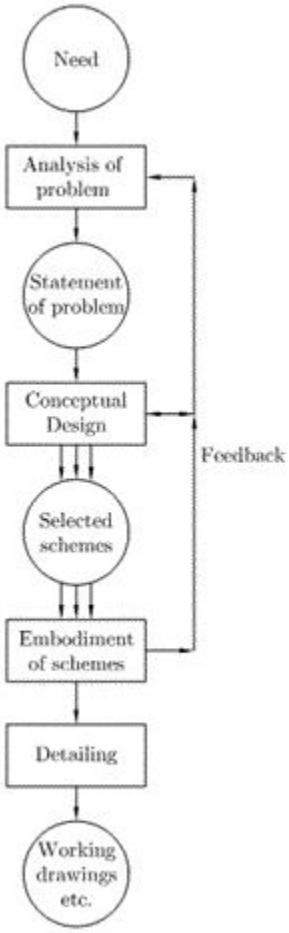

FIGURE 1.1. French Model for the Design Process

FIGURE 1.2. Charlevoix Bridge in Montreal

Once the problem is stated, alternative schemes are produced. First, the concept of biomimetics is introduced. The inspiration of the design comes from the field of biomimetics, where the engineering design of structures is based on the study of biological systems. The first part of the word biomimetics stems from the Greek "bios", which means life, and the second part comes from "mimesis", meaning imitation; hence, "biomimetics" means "imitating life". After many years of observing nature, scientists have explored the principles that govern the natural world, the most important being self-assembly, fitting form to function, self-sustainability and respecting an ordered hierarchy of structures (Benyus, 1997). In an attempt to produce the conceptual design of the bridge under the biomimetics paradigm, what comes to mind, is a structure inspired by natural elements with a hierarchical organization starting from the microstructure up to the superstructure at the macro-level.

The architect Michael Weinstock deduced in his analysis on the evolution of form in nature, how all forms emerge from the dynamic processes by which organized arrangements of material are produced in space and time by natural systems, whether living or non-living (Weinstock, 2010). In his explanation of the dynamics of organization, Weinstock also describes how nature has many integrative levels with hierarchical organization and how self-organized construction and regulation of material forms emerge from the collective behaviour of all the different levels.

"In the morphogenesis of biological organisms, it is the animation of geometry and material that produce form", wrote Hensel, Menges and Weinstock in *Morphogenetic Design Strategies* (Hensel et al., 2004). That is, the material is tailored with a certain geometry to produce the final form of the workpiece. They also added that materials in biological systems are successful mostly because of the way they are put together, rather than because of the materials themselves. The notion of hierarchy in materials is also mentioned in this book, as the global behaviour of a natural system is defined to be the product of all local actions such as sensing, decision-making and reactions.

In particular, it is the structure of trabecular bones that is of interest for the design of this bridge, since it possesses the characteristics of a lightweight and stiff structure. Furthermore, in bone, material is absent in the understressed parts and concentrated in the highly stressed ones (Hensel et al., 2004). However, the structural shape of trabecular bones is marked by a highly complex organization, which makes it complicated to mimic in the design of a bridge. By resorting to cellular materials, such as lattice, the needed characteristics of the trabecular bone, such as low weight and high stiffness, can be achieved alternatively with a material configuration simpler to study. At the same time, this type of material is marked by its multi-scale characteristics, where the behaviour at the macro-scale is dictated by the organization of material at the micro-scale.

In fact, many architects are inspired by nature in the design of their structures. Frei Otto (Otto and Rasch, 1995) and Santiago Calatrava (Tzonis, 1999) are two of these architects, among many others. Their constructions are more integrated in the natural ecosystem than their counterparts because they are created through the perspective of the mechanical and physical processes that form natural objects. This involves combining fields of architecture, engineering, and science. For this to happen, researchers should keep an open mind about the multi-disciplines involved

in the matter. The Lyon airport railway station by Santiago Calatrava, appearing in Fig. 1.3, is one of these architectures, inspired by the skeleton of a bird. Another architecture by Calatrava is the Peace pedestrian bridge shown in Fig. 1.4, featuring an innovative design.

FIGURE 1.3. Lyon Airport Railway Station by Santiago Calatrava

FIGURE 1.4. Peace Bridge in Calgary by Santiago Calatrava

The general shape of our bridge design will resemble that of a curved spine with a cross-section inspired by the spinal cord having two ribs on the sides, as illustrated

in Fig. 1.5. The spine is continuous throughout the bridge, with the ribs located at specified points with a defined thickness. A 3D model of the bridge, displayed in Fig. 1.6, was developed to demonstrate the concept.

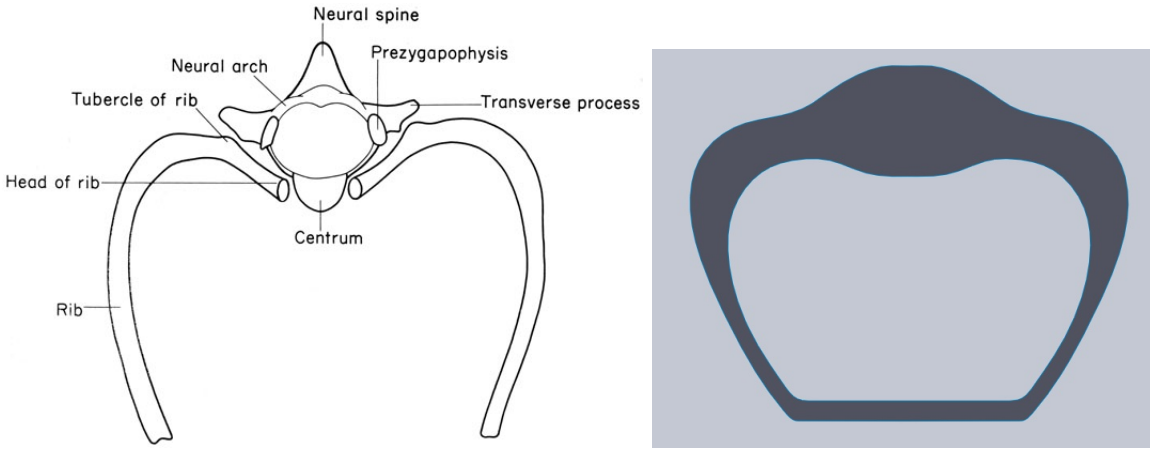

FIGURE 1.5. Geometry of cross-section inspired from that of a spinal cord

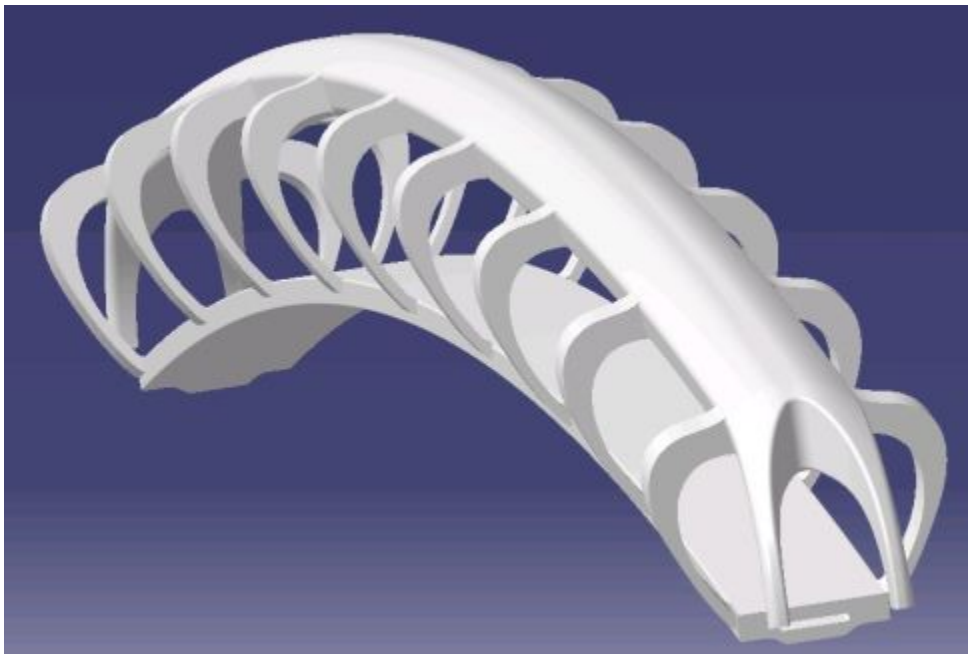

FIGURE 1.6. 3D model of the bridge

The design complexity of the proposed model can be studied in reference to the field of design theory. At the conceptual stage of the French model of Fig. 1.1, the

complexity of one alternative solution can be regarded as the entropy of a thermodynamic system, thus assimilating complexity to diversity. An alternative solution is then considered more complex if its components are more diverse (Angeles, 2007). Diversity is evaluated based on the notion of a function-carrier, which is a component intended to implement a function, namely, a generic task to be satisfied by this component (Pahl and Beitz, 1996). If the carriers of a given function are as identical as possible, the diversity of the system, and hence its complexity is reduced. With regard to the model in Fig. 1.6, it can be decomposed in terms of modules. Individual rib components can represent these modules, as function-carriers fulfilling the task of supporting the spine, which will take the bulk of the load. Designing these ribs in a manner to reduce the complexity of the system will also facilitate and ease the automation of the fabrication process.

At the University of Manitoba, Prof. Lancelot Coar and his students designed a red metal frame supporting a white nestling cocoon, as displayed in Fig. 1.7. This cocoon is one of five warming huts built to provide shelter for skaters in such an unconventional fashion. This structure has been described as an edgy and fierce gesture of architectural design that demonstrates energyzing innovations in the architectural world. The meshing scheme of the metal frame offers a motivation in terms of the design of the pedestrian bridge in this work. From the same outlook, a rendering of the reimagined Oakridge Centre in Vancouver, displayed in Fig. 1.8, features a mall entrance that can also be architecturally interesting and inspiring to this project. The components of this periodic structure are some sort of cellular units with triangular and rectangular cells packed together to yield an artistic form of the entrance.

A most recent example along these lines is a skyscraper design with a lattice-like type of material, introduced during the 9th Annual Skyscraper Competition, as shown in Fig. 1.9.

FIGURE 1.7. Warming hut for skaters in Winnipeg

FIGURE 1.8. An artists rendering of Oakridge Centre in Vancouver

1.1 Bridge Design

In the field of bridge design, many types of bridge models can be adopted, depending on the type of bridge in question. For instance, there are global bridge models that

FIGURE 1.9. Urban Alloy Tower

consider the entire bridge with all its substructures. Those models are primarily used for seismic design. There are also tension and compression models to capture nonlinear responses, and frame models to study portions of a structure between expansion joints. Specifically for slab-beam bridges, two models are available, spine and grillage model. The latter is associated with bridges that cannot be considered rigid, such as very long and narrow bridges; the former is represented with beam elements and is generally used for regular bridges. Our model, that is the spine model, is the one that seems the most appropriate for the pedestrian bridge under design, considering that in static analysis, if the span length exceeds 2.5 times the width of the bridge, the superstructure may be idealized as a single spine beam and the eccentricity of loads should be taken with respect to the centerline of equivalent beams (AASHTO, 2012). This method is to be applied to the analysis of the superstructure of the bridge.

1.2 Materials

As indicated earlier, cellular materials are the most relevant category of material for this research. Nevertheless, prior to discussing the matter of cellular material with lattice microstructure, it is important to elaborate on the more general class of Functionally Graded Materials (FGM). These are among advanced materials characterized by variation in properties over their volume, due to changes in composition and structure. FGMs exist in natural tissue, such as bones and wood. Materials with varying properties are essential in engineering applications where the need of conflicting requirements is increasing; examples of these materials are alloys and composite materials. The revolutionary Functionally Graded Materials offer the possibility to tailor a material for a specific application (Rasheedat and Esther, 2012). As for cellular materials, these consist of a network of interconnected cells that can be represented either by an array of polygons such as squares and hexagons in two dimensions or by a stack of polyhedra in three dimensions, such as foam. A cellular material with periodic lattice microstructure is characterized by a periodic arrangement of a unit cell with specific topology (Gibson and Ashby, 1997).

The most essential parameter of a cellular solid, like the one to be used throughout the project is its relative density. This is defined as the ratio of the density of the cellular material to that of the solid making up the cell walls. The ratio can be visualized as the proportion between cell wall and pore space; as the relative density increases, the thickness of the cell walls increases and the pore size decreases (Gibson and Ashby, 1997). The relationship between relative density ρ and the geometry of a square unit cell is illustrated in Fig. 1.10 (Arabnejad and Pasini, 2012). It is noteworthy that the triangular unit cell is the topology used for the analysis.

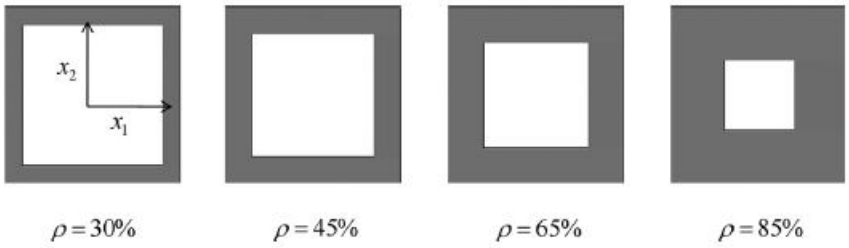

FIGURE 1.10. Square unit cells for different values of relative densities

Due to the high level of complexity in the structure of cellular materials, their analysis is extremely expensive on the computational side using detailed finite element analysis. This problem can be solved through a model relating the macroscopic homogeneous properties of the material to those of the lattice. The process involved is called homogenization, whereby the material is analyzed based on a representative volume element (RVE) of the cellular microstructure. Thus, this method is a multiscale approach, in which the global and the local levels are decoupled. The microstructure is assumed to be spatially periodic, which is ensured by constraining the displacements at opposite sides of the RVE to be equal (Hollister and Kikuchi, 1992). In a periodic lattice, the RVE can be chosen as the unit cell that is tessellated throughout the structure. A descriptive image of the homogenization concept is displayed in Fig. 1.11 (Arabnejad and Pasini, 2012).

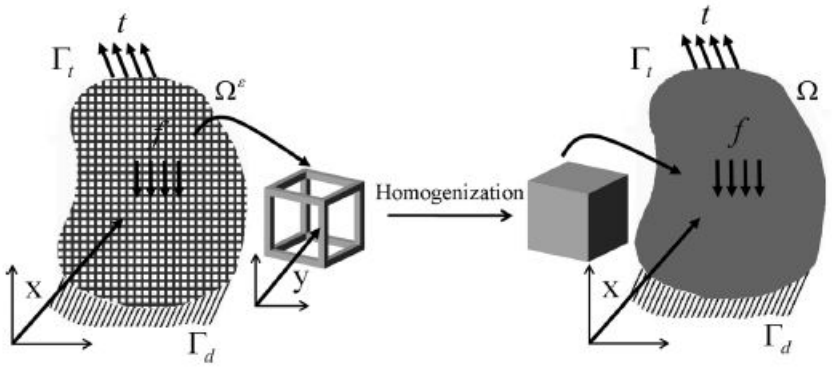

FIGURE 1.11. Description of homogenization concept

Among many homogenization methods, asymptotic homogenization was selected for this project because of both its high accuracy relative to other homogenization procedures and the availability of in-house developed code. Asymptotic homogenization relies on an asymptotic expansion of field quantities such as displacement, assumed to vary smoothly at the macroscopic level. The differential equations with rapidly oscillating coefficients are replaced with differential equations whose coefficients are either constant or slowly varying, in such a way that the solutions are close to the initial equations. An important parameter in homogenization is the magnification factor ϵ that scales the dimensions of a unit cell to those of the medium at the macroscopic level. Some convergence estimates show that the accuracy of the theory is directly related to this factor. Physically, the meaning of this parameter is that quantities like stress or strain will vary $1/\epsilon$ faster on the microscopic than on the macroscopic level (Hassani and Hinton, 1998).

Lattice material with different unit cell topologies have been studied in 2D and 3D, and characterized in the literature using different methods. For 2D unit cells such as square, triangular, hexagonal and others, the lattice structure can be studied using Timoshenko beams and column theories under different loading conditions (Wang and McDowell, 2004), or numerical methods based on long-wavelength Block theory through the implementation of Floquet-Block transformation simultaneously with the Finite Element Method (Chopra, 2011). On the other hand, a matrix-based procedure where the lattice is modelled as a pin-jointed infinite micro-truss structure and homogenized using the Cauchy-Born hypothesis has also been applied (Elsayed and Pasini, 2010). The most pertinent method for this research is that of asymptotic homogenization for the characterization of the unit cells (Arabnejad and Pasini, 2013). The details of this method will be stated later on. Moving on to 3D unit cells some of which are cubic, octahedron and dodecahedron, the leading study relies on

a multiscale approach separating the analysis in two scales, the macroscopic level, where the material is assumed uniform, and the microscopic level, modelled with FE (Vigliotti and Pasini, 2012). The octet truss, a particular cell topology, is examined in depth due to its exceptional characteristics with respect to stiffness (Elsayed and Pasini, 2010).

1.3 Theories

Functionally Graded Materials can be studied through many approaches based on different theories. For instance, a structure made of a FGM can be optimized for a given application using the material volume fractions as design variables. The optimal material properties can then be found by integrating the two design variables in a common objective function represented by a coupled Hamilton-Jacobi equation and a diffusion partial differential equation (Xia and Wang, 2007).

Another method is that of fundamental solutions (MFS) for graded materials in two-dimensional heat conduction problems. In this case, the material can be isotropic or anisotropic, single or composite, and exponentially nonlinear. This type of problems can also be solved using the boundary element method (BEM); however, MFS is easier to implement because no surface integrals need to be calculated. The method consists of solving a linear or nonlinear least-square problem, depending on whether the sources are prescribed or not. In the same field, the domain decomposition technique is also appealing (Berger and Karageorphis, 1999). It replaces layered homogeneous materials by two exponentially graded inhomogeneous materials (Marin and Lesnic, 2008).

An adaptive global-local approach to the analysis of linearly elastic FGMs can be employed. Since the computational analysis of FGMs is highly costly, averaging

techniques are used for the homogenized material model. In this approach, the modelling error of these techniques is estimated and controlled in a systematic manner (Vemaganti and Deshmukh, 2005).

Functionally graded materials are also examined by the parametric finite-volume theory. Unlike the finite-element method, this method enables the modelling of curved boundaries in the structure and eliminates stress concentrations at the corners of rectangular subvolumes. This is done by mapping a reference square subvolume onto a quadrilateral subvolume in the actual discretized microstructure (Cavalcante et al., 2008).

From another perspective, instead of repeating the same unit cell throughout the medium, it can gradually change along one or more directions of periodicity in quasi-periodic composites. This can be done by means of second-order homogenization theory, where the grading at the micro-level is taken into consideration. This method is similar to the one developed for periodic composite materials with rapidly varying macroscopic strain fields as in regions of high gradients.

Briefly, there are many powerful homogenization methods starting with the simple rule of mixture (Voigt or Reuss models), passing by more elaborate methods such as the Mori-Tanaka method and self-consistent method up to the asymptotic homogenization for periodic cellular media (Anthoine, 2009). The latter is the method that will be exploited for this particular project.

1.4 Applications

The main applications of FGMs are in the fields of aerospace, biomechanics, optoelectronics, energy, nanotechnology and tribology.

In the field of biomaterials, living tissue is characterized by its functionally graded properties. For this reason, FGMs find applications in many biomedical devices

such as an artificial biomaterial for knee-joint replacement, titanium implants with a graded biopolymer coating, HAP-collagen I scaffolds, and many others. Scaffolds, in particular, need to have an optimum mechanical behaviour as well as improvement of cell ingrowth, which can be achieved through functionally graded materials (Pompea et al., 2002).

The advantages that can be accomplished with FGMs are numerous and the range of fields that can benefit from these advantages is vast. In construction, as pertaining to the application of bridge design, lightweight structures with optimum performance can be designed by resorting to this class of materials as the building component.

1.5 Fabrication

Several production techniques of Functionally Graded Materials are available. A novel additive manufacturing technology for producing FGMs as three-dimensional parts is Freeze-form Extrusion Fabrication. This technique includes a triple-extruder mechanism, extruder modelling and control, pastes extrusion planning for desired composition gradients, and software coding for motion and extrusion control. Using this process, limestone (CaCO3) parts with graded colors were fabricated (Ming et al., 2012).

Other powder processes and techniques involving metal melts are applied for graded polymer processing. In these methods, modelling of gradient formation, sintering and drying are important for the production of defect-free parts with predictable gradients in the microstructure (Kieback et al., 2002).

The semi-solid forming process (SSF) is an essential production method for FGMs. As an example, a Mn-Sb (Manganese-Antimony) alloy with a hypoeutectic composition was used to produce particle-dispersed composites under magnetic

field gradients using SSF. With this method, the direction associated with an increasing volume fraction of particles can be controlled by adjusting the direction of the field gradient (Liu et al., 2007).

Concerning materials with lattice microstructures, additive manufacturing techniques such as 3D printing and Electro-Beam Melting (EBM) can be suitable candidates for consideration in the case of this particular application. It is noteworthy that all of these fabrication methods are pertinent to the manufacturing of a prototype of the bridge on a small scale. Construction of the bridge at its natural scale will be discussed in the sequel.

1.6 Optimization

The aim of optimization in this research is to devise a structure for the pedestrian bridge characterized by optimal mechanical performance. This can be translated into a structure with maximum stiffness without a compromise in terms of the global weight of the bridge or the entire volume of material making up the bridge. In other words, the objective of the design process is to minimize weight while maximizing stiffness. These are two conflicting requirements, which leads to a multi-objective optimization procedure.

Prior to the discussion of optimization methods and alternatives, it is important to define the nature of the optimization problem under consideration. In fact, the objective functions to be computed can be embodied by weight and stiffness. Hence, explicit formulations of the objective functions are absent. Moreover, neither gradient nor Hessian of the objective function are available. As for the type of evaluation function, type and range of the design variables, and other information specific to the optimization problem, they will all be laid out in the methodology section once the

details related to the design steps have been identified. The optimization method is to be selected first.

Due to the lack of an explicit objective functions as well as its gradient and Hessian, deterministic methods such as gradient methods and Sequential Quadratic Programming (SQP) optimization technique, are out of the question. Stochastic methods, on the other hand, such as the Monte Carlo method and Genetic Algorithms (GA), are more appropriate for this particular case. Furthermore, having multiple objectives, population-based optimization techniques are the most relevant to this problem, since designers are often not concerned with a single point solution but instead with a set of optimal solutions, referred to as the set Pareto-optimal points (Srinivas and Deb, 1995). In this category of population-based techniques, GA are the most popular.

In 1985, Schaffer established a genetic algorithm based on scalarizing the vector of objectives to one function by averaging all the objectives using a weight vector (Schaffer, 1985). His vector-evaluated GA method (VEGA), however, depends on the choice of the weight vector and seems to be biased towards some regions of the solution. This bias can be eliminated by distributing the population over the entire Pareto region as Goldberg suggested in his book (Goldberg, 1989). This suggestion was hinged on the concept of nondominated sorting, which integrates a ranking selection method that emphasizes good points of the solution and a niche method that maintains stable subpopulations of good points. Fonesca and Fleming applied Goldberg's suggestion in their multi-objective GA (MOGA) by checking all the population and assigning to nondominated individuals a first rank. Other individuals are then ranked by a nondominance check relative to the rest of the population (Fonseca and Fleming, 1993). In their comparison of selection schemes used in genetic algorithms, Goldberg and Deb mentioned how MOGA can lead to premature convergence because

of the large selection pressure it produces. Another extension of the Goldberg suggestion was also developed in 1994 based on Pareto domination tournaments (Horn et al., 1994), its inconvenience being its dependence on population size, which results in premature convergence if this size is large, and in few nondominated points if it is small.

The non-sorting genetic algorithm (NSGA) was implemented departing from the same non-dominated sorting scheme of Goldberg and incorporating a niche technique with a speciation method (Srinivas and Deb, 1995). An improvement of the method was also carried out to produce NSGA-II, achieving a better spread of solutions and a convergence near the true Pareto-optimal front compared to other evolutionary genetic algorithms. These include the Pareto-archieved evolution strategy (Knowles and Corne, 1999) and the strength pareto evolutionary algorithm (Zitzler, 1999). NSGA-II fixes previously encountered problems with computation complexity, nonelitism approach and the need for specifying a sharing parameter (Deb, 2002). This optimization method was selected for the minimization of weight and maximization of stiffness of the bridge to be designed.

1.7 Mapping

To reach the manufacturing stage, a CAD file is needed. As such, the final geometry has to be produced in 3D, which requires the translation of the optimum resulting relative density distribution to the corresponding lattice microstructure, sometimes referred to as the mapping procedure. One possible method of developing the mapping procedure is through a code that creates the pores of the lattice material as holes in the solid geometry through the macros of a CAD software package such as SolidWorks macros. An alternative is the 3D modeler Rhinoceros, running a Python

script, including all the commands for creating the geometry.

In Chapter 2, the methodology to design and optimize the lattice structure of the bridge is detailed based on the different scales involved in the process. The third chapter displays the results of each of these scales as well as those of the mapping and additive manufacturing. Finally, the last Chapter includes discussion and conclusions before ending the thesis with recommendations for future work.

CHAPTER 2

Methodology

Considering the relative density of the lattice material as the design variable of interest, asymptotic homogenization has to be coupled with an optimization algorithm. An optimum relative density distribution is then obtained throughout the bridge. The desired goals, such as maximizing the global stiffness of the structure and minimizing its weight, are then met through this optimum distribution.

To reach this outcome, the problem is divided into two components. The first, *system*, corresponds to the superstructure of the bridge in 3D, the second, *component*, is related to the cross-section of the bridge in 2D. The analysis on the system scale is initially conducted to obtain the working loads on each cross-section of the bridge. These loads are then transmitted to the component level, where optimization is applied and the optimal relative density distribution is calculated. The detailed methodology for each level is laid out in the coming sections. First, the design requirements of the bridge are defined. At the end, the method implemented to produce prototypes using additive manufacturing is described. A flow chart describing the methodology is displayed in Fig. 2.1.

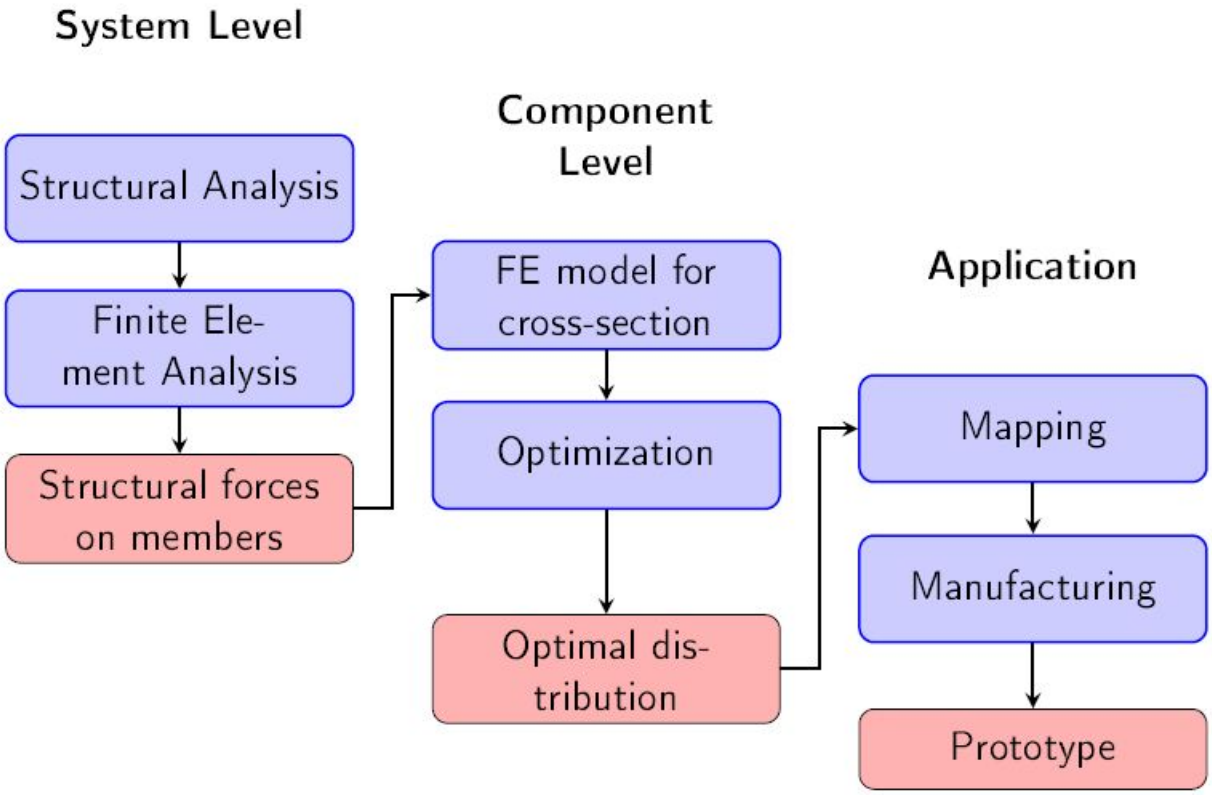

FIGURE 2.1. Methodology flow chart

2.1 Design requirements

The geometrical parameters of the bridge are calculated based on standard specifications for pedestrian bridge design (CSA, 2006).

(i) Bridge Entrance

A width of 3.5 m is selected based on the minimum standard width accommodating a family of four people.

A height of 3.33 m is selected based on the maximum height of a person and the minimum allowable personal space.

(ii) A height of 4 m is selected for the arch based on the average height of trains (2.7 m) with an extra allowance for electric cables.

(iii) The maximum allowable slope for a ramp is 8.33%. Taking this value into account, a span length of 80 m was selected for the 4 m arch height.

2.2 System

This is the level associated with the superstructure of the bridge in 3D shown in Fig. 2.2 including the spine and the rib components. Investigation on this scale is dependent on the structural analysis that results in the proper geometry specifications related to the number and thickness of the ribs. With the proper design, internal forces required at the component level can be deduced.

FIGURE 2.2. System level

2.2.1 Structural Analysis. In order to design the pedestrian bridge to withstand the applied loads, a structural analysis of the bridge is required. With reference to Section 1.1, the model that fits the bridge under discussion the best, is the spine model. This model designates the spine as the main structural component taking the major part of the load. Even so, considering the distinctive shape of the ribs, determining exactly the amount of load they carry is extremely challenging. Hence, it is convenient to account for the rib components in the structural analysis and not only the spine, which dictates modelling the full bridge in 3D. At this stage, the geometry of the cross-section, as well as the arch height and the span length, have been already fixed by the design specifications for pedestrian bridges. By specifying a fixed rib thickness of 1 m and varying the rib span, the appropriate number of ribs

can be obtained based on the minimum allowable rib span. This is achieved through an iterative procedure outlined in the steps below.

(i) An initial CAD model of the bridge in 3D was created, assuming a given number of ribs equal to nine along the whole span. This translates into four ribs on each side of the mid-plane of symmetry, and one rib exactly at that plane.

(ii) The model is then subjected to FEA with load combinations for Ultimate Limit States (ULS), based on the National Building Code of Canada (Beaulieu et al., 2003). Ultimate states include exceeding the loading-carrying capacity, overturning, sliding, and fracture. As such, these states involve applying amplifying factors on loads and reducing factors on stresses. Principal load combinations are $1.35D$, $1.25D+1.5L$, $1.25D+1.5S$ and $1.25D+1.4W$, where D stands for dead load, the weight of the structure; L represents the live load, that of the pedestrians as well as other factors such as service vehicles; S is for snow, including ice and associated rain; and W is the variable load due to wind.

Values for these load components were obtained from CSA for the city of Montreal. The live load is equal to 4 KPa (CSA, 2006), the snow load to 2.6 KPa and the wind load to 0.42 KPa (CCBFC, 2010). The load combination among the previous list that produces the largest load is selected and applied on the model of the bridge.

In FEA, boundary conditions were applied by clamping the bridge at both ends and the pedestrian load was applied as a uniformly distributed load.

(iii) Internal moments and forces were obtained at the cross-sections corresponding to the rib placements in addition to the resulting vertical displacement at these locations.

The maximum deflection at mid-span is compared with the allowable value for bridges, which is obtained from serviceability limit states for the AASTHO criteria (FHA, 2011). The graph shown in Fig. 2.3 plots the relationship between the allowable deflection limits for a given span length of the bridge. For a span length of 80 m, with the proper dimension conversions, the allowable deflection is approximately equal to 0.95 mm.

The maximum loads are compared with the failure strength which is the smaller value between the yield and fracture strength, after application of the reduction factors. The failure criteria are:

$$\phi_t P_n = 0.9 A_g F_y$$

$$\phi_t P_n = 0.75 A_c F_u$$

The reduction factor on the fracture limit is smaller than that on the yield limit because of the unpredictable nature and more serious consequences of failure due to fracture than yield.

(iv) If the design fails, the rib span is decreased, that is the number of ribs is increased. The model is then updated and a new iteration is conducted. Otherwise, if the design is suitable, the process is stopped and the calculated loads are transferred to the component scale.

2.3 Component

The component level consists in studying the relative density distribution at the cross-section level in 2D until an optimal solution is reached. As discussed in Section 1.2, asymptotic homogenization will be used in this work for the analysis of the

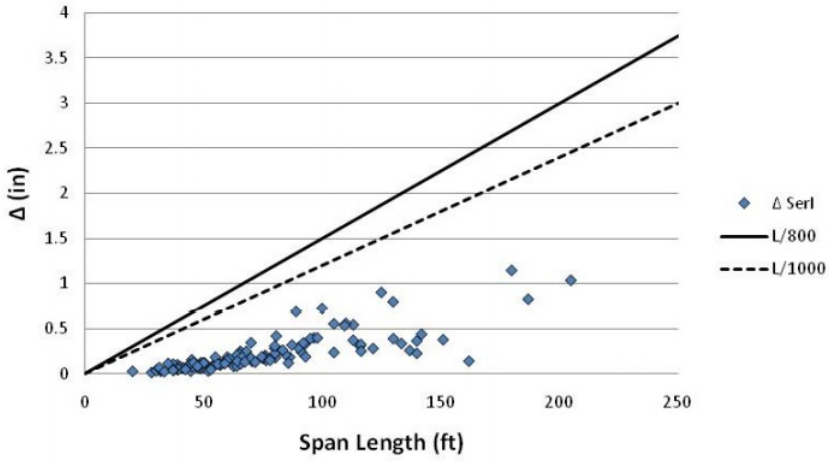

FIGURE 2.3. Service I Deflections vs. Span Length for Simple Spans

lattice material. This theory approximates physical field quantities like displacement, u, by a power series expansion with respect to the magnification factor ϵ (Hollister and Kikuchi, 1992):

$$u^{\epsilon}(x) = u_0(x,y) + \epsilon u_1(x,y) + \epsilon^2 u_2(x,y) + ... \tag{2.1}$$

where $u_0, u_1, u_2...$ are periodic functions with respect to the coordinate y. Deriving eq. (2.1) with respect to x and using the chain rule while neglecting higher order terms, the small deformation strain tensor is obtained (Arabnejad and Pasini, 2013):

$$\{\epsilon(u)\} = \frac{1}{2}(\nabla u_0^T + \nabla u_0)_x + \frac{1}{2}(\nabla u_1^T + \nabla u_1)_y \tag{2.2}$$

The first term is the gradient of the field quantity with respect to the global coordinate system; it represents as such the average or macroscopic strain $\{\bar{\epsilon}(u)\}$. The second term is the gradient of the field quantity with respect to the local coordinate system; it is then the periodic fluctuating strain $\{\epsilon^*(u)\}$ at the microscale level. Its periodicity is ensured by setting equal nodal displacements on the opposite edges of the RVE.

Substituting eq.(2.2) into the standard weak formulation of the equilibrium equations gives:

$$\int_{\Omega^\epsilon} \{\epsilon^0(v) + \epsilon^1(v)\}^T [E] \{\bar{\epsilon}(u) + \epsilon^*(u)\} d\Omega^\epsilon = \int_{\Gamma_t} \{t^T\}\{v\} d\Gamma \tag{2.3}$$

where $\epsilon^0(v)$ and $\epsilon^1(v)$ are the virtual macroscopic and microscopic strains, respectively, [E] is the local elasticity tensor, and {t} is the traction at the traction boundary Γ_t. Integrating eq. (2.3) over the RVE volume and assuming that the virtual displacement $\{v\}$ is constant on the macroscopic level, the microscopic equilibrium equation becomes:

$$\int_{V_{RVE}} \{\epsilon^1(v)\}^T [E] \{\epsilon^*(u)\} dV_{RVE} = -\int_{V_{RVE}} \{\epsilon^1(v)\}^T [E] \{\bar{\epsilon}(u)\} dV_{RVE} \tag{2.4}$$

Using finite element discretization, eq. (2.4) simplifies to:

$$[K][D] = [F] \tag{2.5}$$

where [K] and [F] are the global stiffness matrix and force vector, respectively, obtained through the sum of the elemental stiffness and force components given below:

$$[k^e] = \int_{Y^e} [B]^T [E] [B] dY^e \tag{2.6a}$$

$$[f^e] = \int_{Y^e} [B] [E] \{\bar{\epsilon}(u)\} dY^e \tag{2.6b}$$

where [B] is the strain-displacement matrix.

Equation (2.5) combined with the assumption of small deformation and material elasticity, yields a linear relation between the macroscopic and microscopic strains,

$\{\epsilon(u)\}$ and $\{\bar{\epsilon}(u)\}$, respectively:

$$\{\epsilon(u)\} = [M]\{\bar{\epsilon}(u)\} \tag{2.7}$$

where [M] is the local structural tensor, which can be calculated once $\{\epsilon(u)\}$ and $\{\bar{\epsilon}(u)\}$ are known. The fluctuating strain $\{\epsilon^*(u)\}$ is evaluated based on the matrix [B] and used to calculate the microscopic strain from eq. (2.2) with the given macroscopic strain. The latter is also substituted in eq. (2.6b) to obtain the force vector; microscopic displacements are then determined through eq. (2.5), and the tensor [M] can then be obtained. The microscopic stress is integrated over the RVE to yield:

$$\bar{\sigma} = \frac{1}{|V_{RVE}|}\int_{V_{RVE}} [E][M]dV_{RVE}\bar{\epsilon} \tag{2.8}$$

The effective stiffness matrix is then derived from eq. (2.8):

$$[E]^H = \frac{1}{|V_{RVE}|}\int_{V_{RVE}} [E][M]dV_{RVE} \tag{2.9}$$

The effective mechanical properties of the homogenized material, such as yield strength, can then be obtained using the homogenized stiffness matrix relating the macroscopic strains to the macroscopic stresses. The theoretical background of asymptotic homogenization described above, is implemented through in-house developed MATLAB codes, used in the analysis of the bridge at the component level.

The steps below show the approach adopted for the analysis at this scale, coupling asymptotic homogenization with optimization.

(i) Apply loads obtained from the system level at each cross-section and create a FE model in 2D for half of the geometry (Exploiting symmetry).

(ii) Assume the cross-section is designed as a lattice microstructure with triangular unit cell

Microscopic geometrical parameters are defined in terms of the thickness of the walls of the triangular unit cell.

Asymptotic homogenization is applied based on this specified cell topology.

(iii) Divide the domain into a discrete set of sampling points appearing in Fig. 2.4 as small squares superimposed on the FE mesh

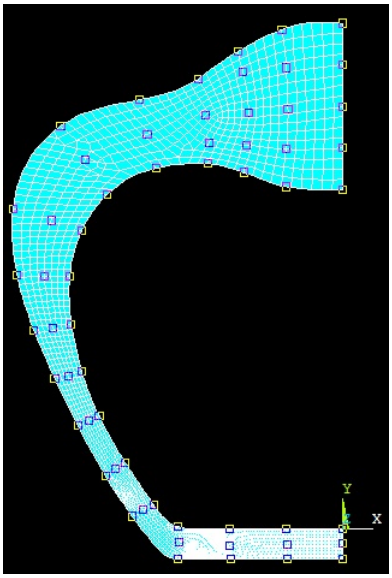

FIGURE 2.4. Location of sampling points on the cross-section

A number of 47 sampling points was selected and the points were distributed so that the entire domain of the surface is covered as uniformily as possible and a minimum number of three sampling points is placed at the thinnest part of the cross-section for appropriate representation.

The relative density values at the sampling points will be the design variables of the optimization problem.

(iv) Obtain the relative density of each element in the FE mesh based on the relative density of sampling points

Assume that each four sampling points form a quadrilateral element

Identify the location of each element of the mesh with respect to the appropriate quadrilateral element of the sampling points

Express the location of the finite element centroid in terms of the location of the four sampling points related to the identified quadrilateral element through shape functions:

$$x_C = \sum_{i=1}^{4} N_i x_i, \quad y_C = \sum_{i=1}^{4} N_i y_i \tag{2.10}$$

where x_i and y_i, for i = 1,2,3,4, are the coordinates of the sampling points forming the quadrilateral element.

Use shape functions for a four-node bilinear quadrilateral element in natural coordinates ζ and η shown in Fig. 2.5:

$$N_1 = \frac{1}{4}(1-\zeta)(1-\eta), \quad N_2 = \frac{1}{4}(1+\zeta)(1-\eta) \tag{2.11a}$$

$$N_3 = \frac{1}{4}(1+\zeta)(1+\eta), \quad N_4 = \frac{1}{4}(1-\zeta)(1+\eta) \tag{2.11b}$$

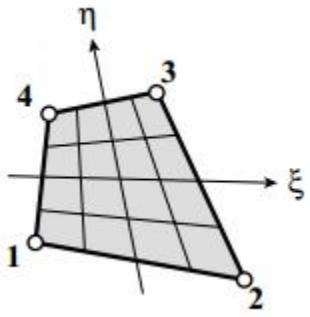

FIGURE 2.5. The four-node bilinear quadrilateral element in natural coordinates

Substitute expressions (2.11) in eqs. (2.10) and obtain the values of ζ and η that satisfy simultaneously the two equations of x_C and y_C

Calculate shape functions for each element using the computed values of ζ and η

Rewrite the expressions for x_C and y_C of eqs. (2.10) for the relative density:

$$\rho_C = \begin{bmatrix} N_1 & 0 & N_2 & 0 & N_3 & 0 & N_4 & 0 \end{bmatrix} \begin{bmatrix} \rho_1 \\ \rho_2 \\ \rho_3 \\ \rho_4 \end{bmatrix}$$

Determine the relative density value for each element using previously calculated shape functions

(v) Calculate mechanical properties (in this case, Young's modulus, Poisson's ratio and shear modulus) using asymptotic homogenization theory based on the relative density distribution found in the previous step

Results are obtained at discrete points appearing on the graph in Fig. 2.6 and the least-square method is used to obtain continuous expressions for properties as a function of relative density (Arabnejad and Pasini, 2012).

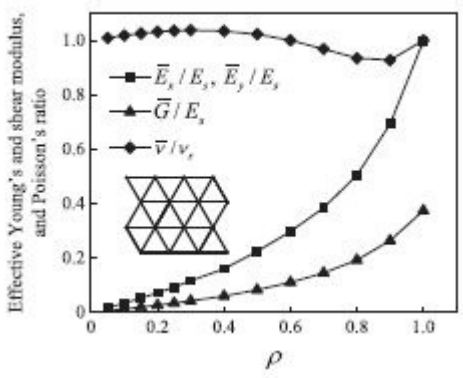

FIGURE 2.6. Material properties for triangular unit cell obtained using asymptotic homogenization

(vi) Input computed properties to a FE solver to determine average stresses and strains through the whole structure

(vii) Evaluate optimization functions and constraints

Results from the FE solver based on macroscopic stress are used to calculate weight and deflection values for the optimization functions as well as von Mises stress value for the constraint on failure.

(viii) Use the NSGA-II algorithm for multi-objective optimization; the formulation of the optimization problem is:

$$\begin{aligned} \underset{\vec{x}}{\text{minimize}} \quad & [mass(\vec{x}), deflection(\vec{x})] \\ subject \quad to \quad & \sigma_{vM} - \sigma_{all} \leq 0 \\ over \quad & 0.1 \leq \vec{x} \leq 1 \end{aligned} \tag{2.12}$$

The number of design variables is 47, representing relative density at the sampling points.

A population size of 150 was designated (about three times the number of design variables).

A total number of 15000 iterations was chosen to allow at least 100 iterations for all populations.

The initial guess for design variables was generated randomly.

Both weight and deflection are minimized with a failure constraint based on von Mises stress.

2.4 Mapping

As noted earlier, what is called mapping is transforming theoretical values of relative density of each unit cell of the lattice material into actual geometry with defined unit cell topology, size and porosity. Two preexisting possibilities to perform

the mapping process are using SolidWorks macros in conjunction with MATLAB, and Rhinoceros in parallel with Python. Details, advantages and disadvantages of each of these alternatives will be discussed hereafter.

2.4.1 SolidWorks and MATLAB. In this case, the boundary of the geometry is produced in SolidWorks or imported from another CAD software package; it is treated separately from the interior constituents of the lattice material, which are created by running SolidWorks macros that perform Boolean operations. These macros are the output of a MATLAB code, where the cell wall thickness for a given unit cell topology is specified, and the pore size is calculated accordingly. Pores with defined shape and size are then produced by subtractive operations from the original homogeneous surface. Superimposing the resulting porous surface with the boundary gives the final lattice structure.

2.4.2 Rhinoceros and Python. As for this method, it is in direct correspondence with FEA. In summary, FE data are read through a Python script, while element geometry and connectivity are established through Rhino commands within the script, thereby allowing the creation of the lattice material. The details of this method are recorded below. It has to be mentioned that an earlier version of this script was provided by the School of Architecture. The script was corrected and updated to incorporate more advanced features. Its efficiency was also improved by introducing new aspects at the preprocessing level, as outlined below.

(i) Data entry

This requires FE data from the mesh produced on the component scale analysis, as well as the results in terms of the optimal relative density data calculated for each element. These should be rearranged in the form of three text files, read at the beginning of the Python script. The files contain the following information:

- Node locations
- Element connectivity table
- Relative density value at element centroids

Data from the text files are read and stored in lists, then items corresponding to each element will be extracted when needed at later stages of the code.

(ii) Preprocessing

The first version of the code included the mapping procedure for lattices with two types of elements, tetrahedra and hexahedra. With the updated version, two additional types were introduced, prisms and pyramids.

For each type of element, the vertices were placed in correlation with node locations, and the outer faces were defined in terms of their attached vertices. There are two possible face configurations for the element types in question; triangular or square. For each face, the correct numbering and sequence of vertices were defined based on FEA conventions specific to the element type.

A full solid element can then be constructed with the corresponding vertices and faces. However, what is needed is a porous element, where the pore size is derived from the relative density value affiliated with that element. Therefore, the vertices related to the pore have to be identified by proper scaling of the outer vertices of the element. This is done through a separate function where coordinates of each vertex are scaled linearly using the relative density value, noting that a different scaling relationship can be applied such as logarithmic or higher-order polynomial. The effect of

this relationship on the accuracy of the mapping is to be investigated in the future.

Upon calling this function, the scaled vertices on each face are then located, as well as the scaled vertices of the whole element. Those two sets of vertices will then be used to form the pore by their proper connections.

Using the scaling scheme described above, if neighboring elements have different relative densities, discontinuities will emerge at the common face between the two elements. This is due to the sharp variation of the geometry between one side of the common face and the other. Moreover, discontinuities are highly undesirable since they make the model defective and ineligible for additive manufacturing. To resolve this issue, a smooth transition in the geometry between neighboring elements has to be established. This can be accomplished by specifying an average value of relative density at the common face between the distinct relative densities assigned to each of the two elements. Before this is done, faces that are common between two elements, which can be referred to as connecting faces, have to be identified.

In the early version of the code, this was done in the Python script itself, by looping through all element lists and comparing the node numbers corresponding to each element, until three common nodes were found for triangular faces and four for square faces. The common faces are then added to the appropriate element list for future extraction in the processing phase. This procedure was quite cumbersome and inefficient, since it considerably increased the running time of the code, having to loop through all the elements at each iteration. This can be avoided by storing the information found at each iteration, to skip unnecessary operations performed

for elements whose common faces have already been identified through the iteration of another element. That was applied via an efficient MATLAB script reading the element connectivity table of the FE data and outputting a text file with the common faces listed next to the indices of the two elements under consideration. This file is in turn read in the Python script and the connecting face data were joined at the proper placement inside the element lists. The process reported significantly reduces the computation time and prevents possible crashes in the software that happened occasionally with the earlier version for a large number of elements.

(iii) Processing

In this part, the geometry is created based on the data gathered and produced in the previous phase. First, the relative density at the connecting faces is calculated by retrieving the relative densities of each of the two involved elements and averaging them. Then, three different layers are defined; one for all vertices, a second for all connecting faces and a third for the remaining faces that are attached only to one element. Those are referred to as cap faces and represent the surface cover of the whole part. Finally, a function is called to place the points and draw the faces in an integrated meshing procedure for each element type.

Briefly, both methods can perform the mapping procedure. However, for the first case, which is not FEA-dependent, only 2D surfaces can be mapped, and the method has to be extended to fit the case of 3D solids. Besides, it is only convenient for straight edges, since on curved boundaries there will be a cutting operation that will create floating edges instead of complete unit cells. On the other hand, the second method is FEA-dependent, which allows perfect mapping between the FE mesh and

the lattice unit cells. This includes mapping in 3D, as well as building unit cells adjusted to the boundary in coordination with the mesh from FEA. Considering that the geometry of the cross-section of the bridge is almost entirely made of curved edges, the second method is selected for mapping the relative density distribution to the lattice geometry.

2.5 3D printing

A proof of concept of parts of the bridge can be built with additive manufacturing techniques. Two 3D printers are available at LIPHE (Laboratory for Integrated Prototyping and Hybrid Environments) of the School of Architecture. The first is Objet500 Connex, with a build size of 490×390×190 mm, and the second is UP plus 2 with a smaller build size of 140×140×135 mm. Both can produce parts having a minimum member thickness of around 1 mm. Although the UP plus 2 cannot produce parts as large as the Oject500 Connex, its advantage is the absence of support material. That is, there is no need for cleaning by removal of support material as is the case with the first printer. This eliminates chances of breaking any member during the cleaning, and ensures a clear porous inner structure of the lattice. However, the usage of support material provides better quality for the printed product.

Summarizing, there are two constraints governing the printing process: the maximum build size and the minimum strut thickness the machine can achieve. As for the lattice material for half the cross-section of the bridge, it was designed at the natural scale with dimensions in meters. For printing, the model has to be scaled down, while satisfying the two constraints mentioned earlier. This is difficult to accomplish, as scaling down the whole model, even to fit the largest printer, makes the minimum member thickness around 0.3 mm. For this reason, only a piece of the cross-section

can be produced in the largest of the two 3D printers. This will be displayed in Chapter 3, along with the other results of the Methodology section.

CHAPTER 3

Results

This chapter presents the results obtained with the method introduced in Chapter 2, at both the system and component scales. Initially, the results of the structural analysis at the system scale will be revealed. Subsequently, FEA results for the final bridge model also on the system scale will be disclosed. Afterwards, optimization and mapping results at the component scale will be reported and, finally, 3D printing results will be outlined.

3.1 Structural Analysis

The strategy that has been devised for the structural analysis of the bridge was described in Chapter 2. The first measure was to create an initial design with nine total ribs along the whole span length.

From the list of load combinations, $1.25D + 1.5L$ is the one producing the largest load after application of the numerical values for the live, snow and wind loads. Thus, performing FEA with one quarter of the geometry, considering the two planes of symmetry along the longitudinal and transversal directions, and applying the selected load combination, produces a maximum mid-span deflection of 0.047 m, and a maximum von Mises stress of 285 MPa. With respect to the allowable deflection

criteria for failure, the model holds. On the other hand, the design fails with respect to the allowable stress criteria, as the von Mises stress exceeds the design strength equal to $0.9F_y$=225 MPa, considering F_y=250 MPa and F_u=460 MPa for steel.

The model is then updated by increasing the number of ribs to 11, adding one rib at each side of the mid-plane of symmetry. The same procedure is repeated, the design in this case being suitable, as it exhibits a maximum deflection of 0.042 m and a maximum von Mises stress of 186 MPa. The FEA results for this model are shown in Section 3.2. They are used to determine internal loads and moments on chosen cross-sections, where optimization will be conducted at the component scale.

The geometry was modelled in CATIA and an IGES version was imported to ANSYS Workbench, then subjected to FEA.

3.2 Finite Element Analysis

The vertical deflection results for the last model with 11 ribs is shown in Fig. 3.1. The rib at the mid-span of the bridge was selected for the design of the lattice microstructure at the component scale. This demands obtaining all load components on the surface of this specific rib. Results from ANSYS Workbench were transferred to ANSYS APDL for post-processing; the internal loads and moments were extracted with the numerical values given below:

$$F_x = 65.465 \text{ KN}, \quad F_y = 393000 \text{ KN}, \quad M_x = 31500 \text{ KNm},$$

where x and y are respectively the horizontal and vertical coordinates in the plane of the cross-section.

3.3 Optimization

At this point, the method switches to the component scale, whose purpose is to produce an optimal relative density distribution for the cross-section of the bridge.

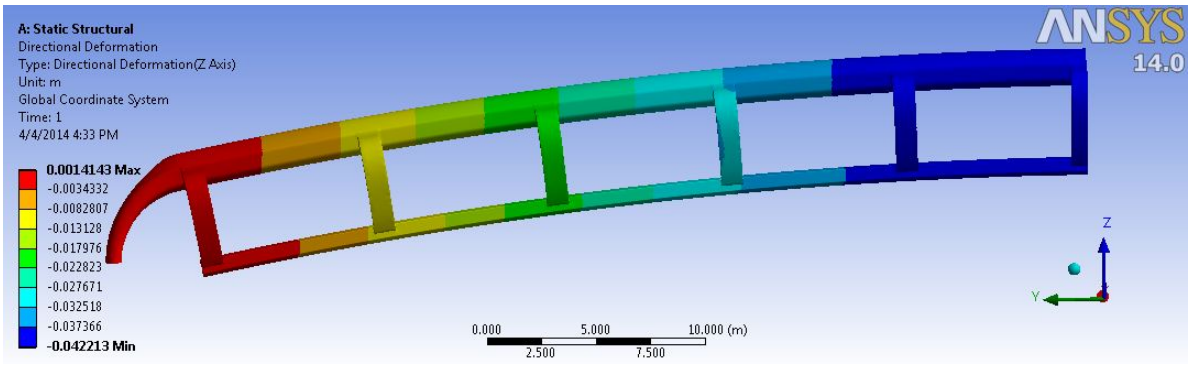

FIGURE 3.1. Vertical deflection

It has already been explained how the entire procedure hangs on an optimization process for a 2D model of the cross-section, where function evaluation is conducted through stress analysis.

Results for the population data of the optimization problem can be visualized by means of a Pareto front, plotting each objective function on a different axis to emphasize their conflicting nature. In fact, a Pareto front is a plot for the nondominated set of solutions. Those are the ones that cannot improve one objective function without worsening the other. The two anchor points representing the extremes of the plot, correspond to a 100% weight for one function and 0% for the other. The desired solution can be chosen depending on the designer requirements.

The Pareto front resulting from this multi-objective optimization procedure is shown in Fig. 3.2. The two objectives, mass and deflection, were normalized with respect to their ranges, m_B-m_A and d_A-d_B respectively, where A and B are the anchor points. This results in nondimensional coordinates on the axes of the Pareto front.

The solution with the minimum possible mass at point A, which results in the largest deflection (100% weight for the mass objective and 0% weight for the deflection objective), was selected for visualization purposes. In other words, the mapping and manufacturing processes were demonstrated for this design solution. Prior to this, a color map was produced using the software Paraview. It is shown in Fig. 3.3, along

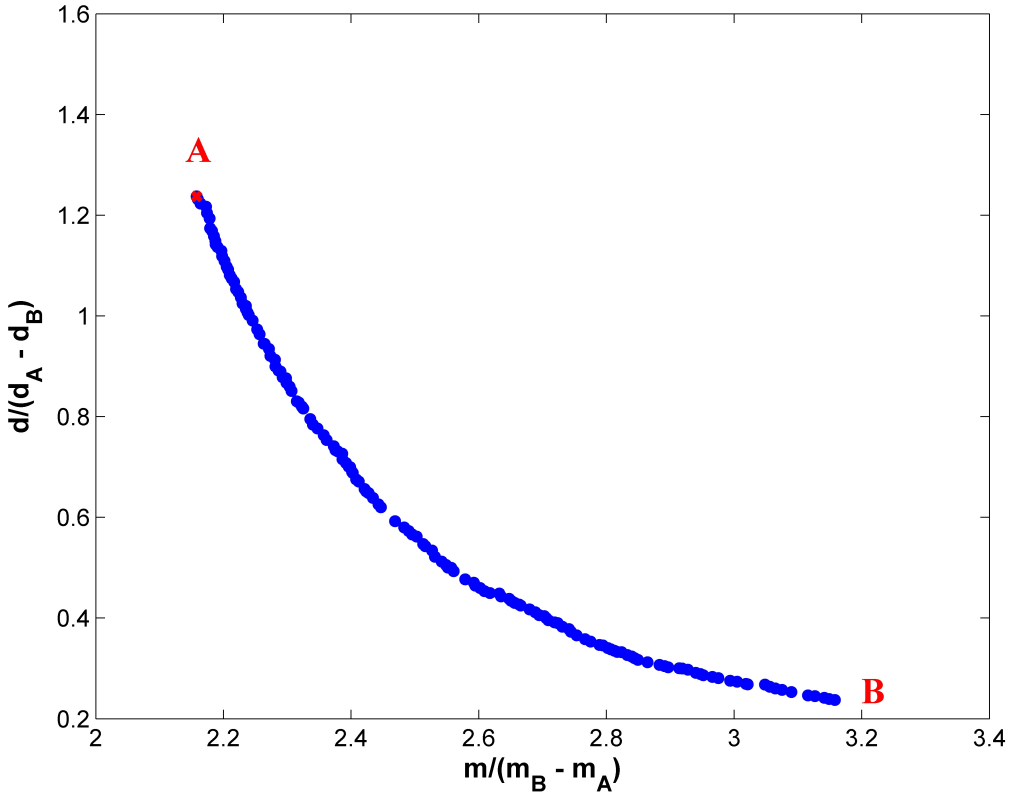

FIGURE 3.2. Pareto Front

with the relative density scale. White regions manifest a lowest relative density of 0.1, while an increasing darkness suggests denser regions with higher relative density values.

3.4 Mapping

The Python script detailed in Chapter 2, was run with the data obtained for the selected optimal solution of the previous section. The lattice structure depicting this solution appears in Fig. 3.4. As seen in this figure, triangular elements were employed within the mapping process. A close-up on the spine zone was placed on the right of the figure for clear observation of the lattice. Also, this piece of the cross-section will be manufactured using the 3D printer.

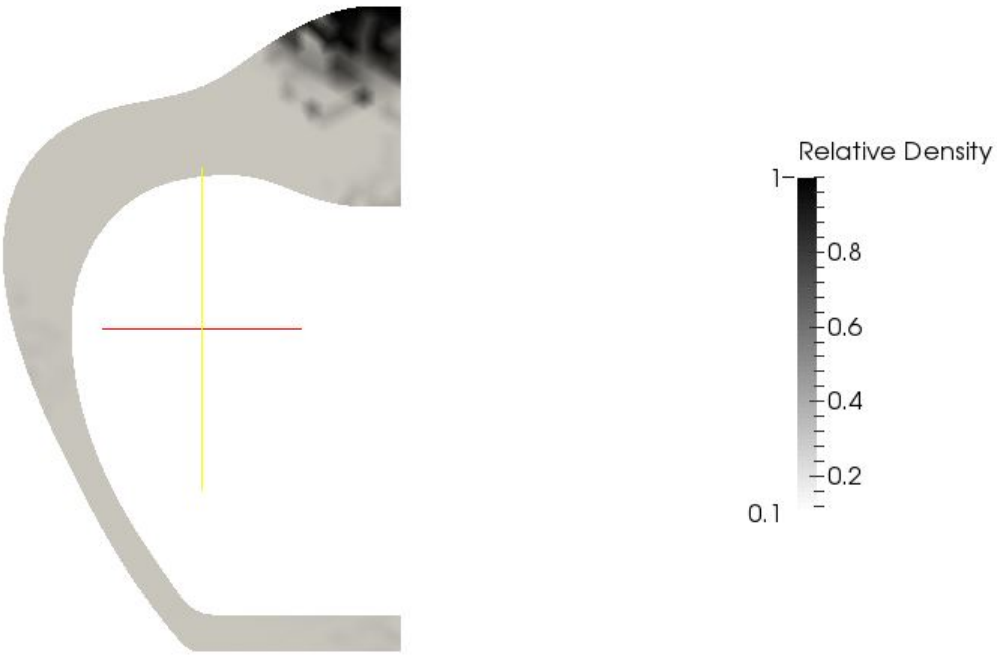

FIGURE 3.3. Color Map of Solution A

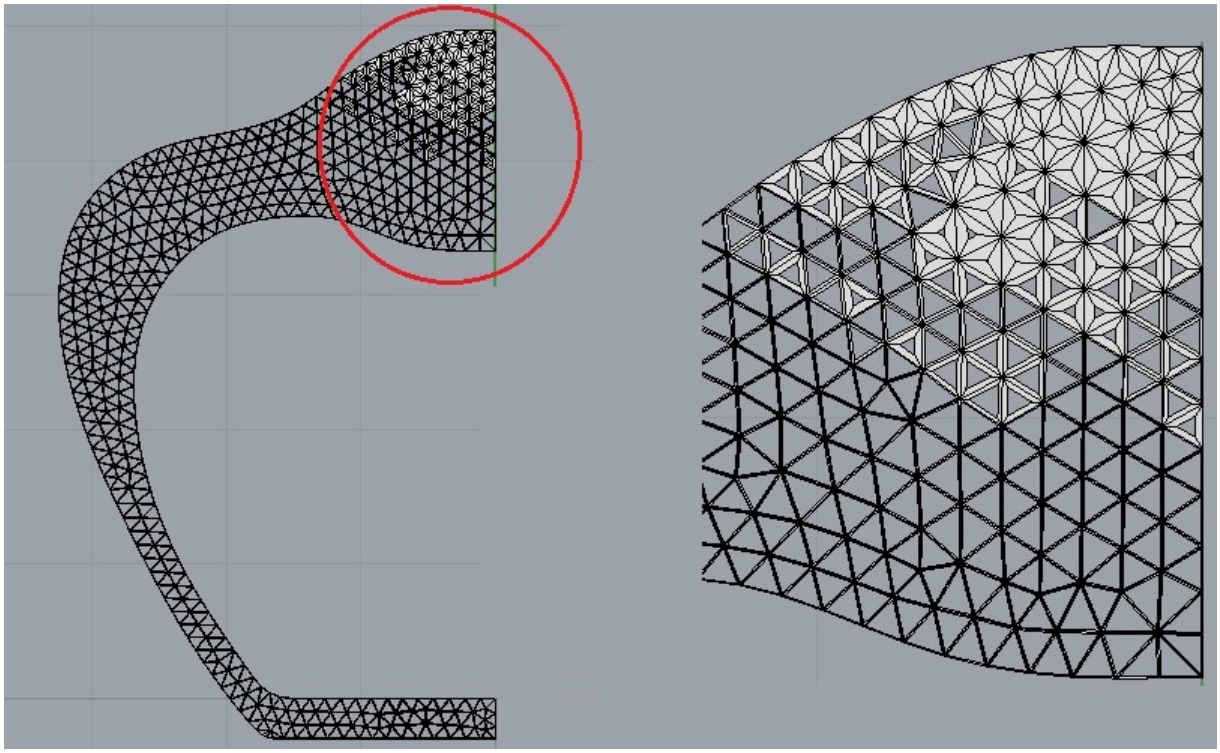

FIGURE 3.4. Lattice Microstructure

The lattice of the cross-section demonstrates the ability of mapping in a plane. Figures 3.5, 3.6 and 3.7 demonstrate the mapping method in 3D. In Fig. 3.5, two different relative density values are exploited for a tetrahedron element, highlighting the variation of pore and cell wall sizes with respect to changes in relative density. In the second figure, the four element types (hexahedron, tetrahedron, prism and pyramid) appear connected together, both with similar and different relative densities. The latter case points out the transition in relative density at the common face between the cube and the pyramid in order to establish a smooth connection. As for Fig. 3.7, a torus with a uniform relative density of 0.5 was mapped using all element types simultaneously, thereby proving the possibility of combining distinct topologies in the same structure.

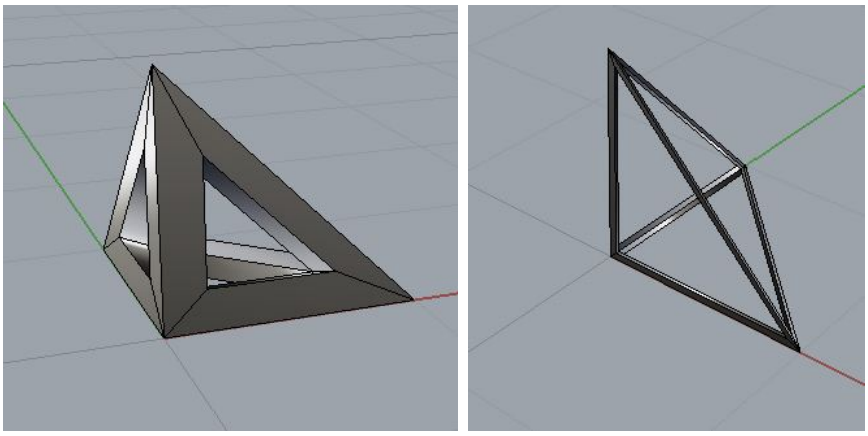

FIGURE 3.5. Tetrahedron element with 0.5 (left) and 0.1 (right) relative density

3.5 3D printing

Revolving around the description of the additive manufacturing process in Chapter 2, the spine portion of Fig. 3.4 was printed using the Objet500 Connex at LIPHE. Pictures of the acquired lattice are displayed in Fig. 3.8 and 3.9, the former at the termination of the printing process with the support material still embedded in the

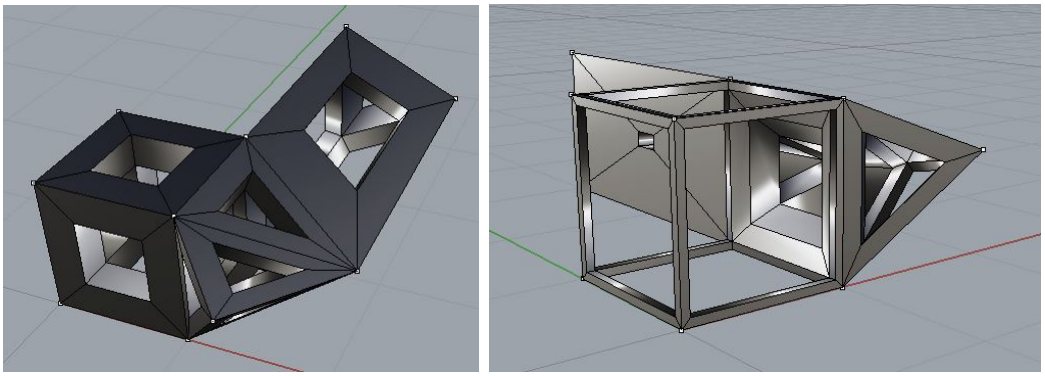

FIGURE 3.6. All element types with identical (left) and different (right) relative densities connected together

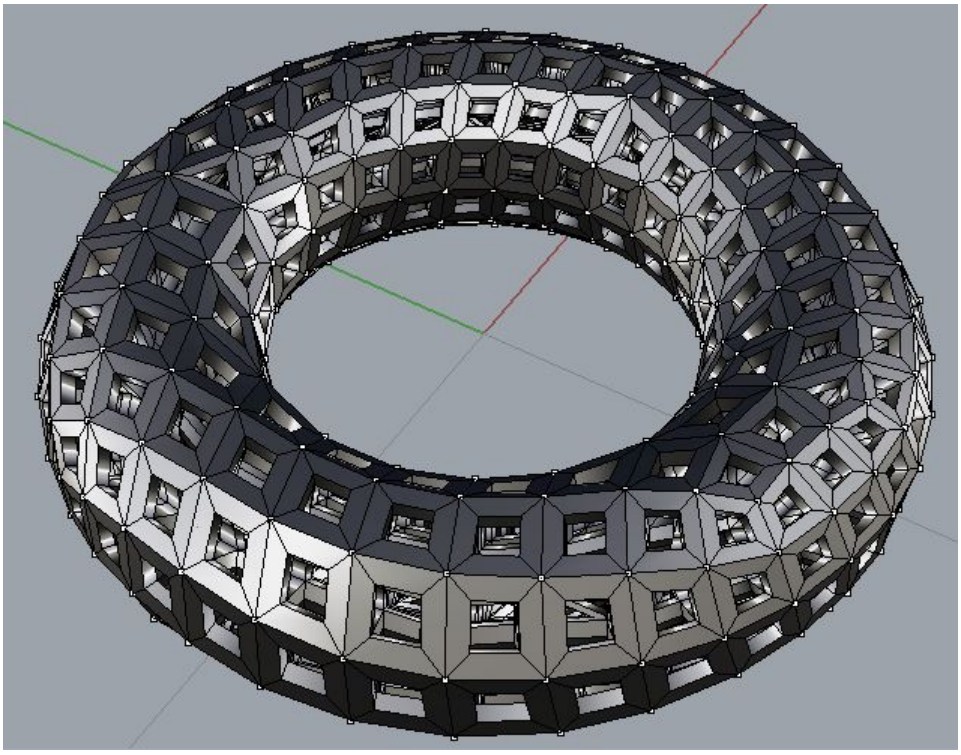

FIGURE 3.7. A torus mapped with quadrilateral elements

part, the latter after cleaning. Along the thickness of the piece, the lattice was only extruded to produce a 3D model, i.e., there is a uniform representation of the lattice along the out-of-plane direction.

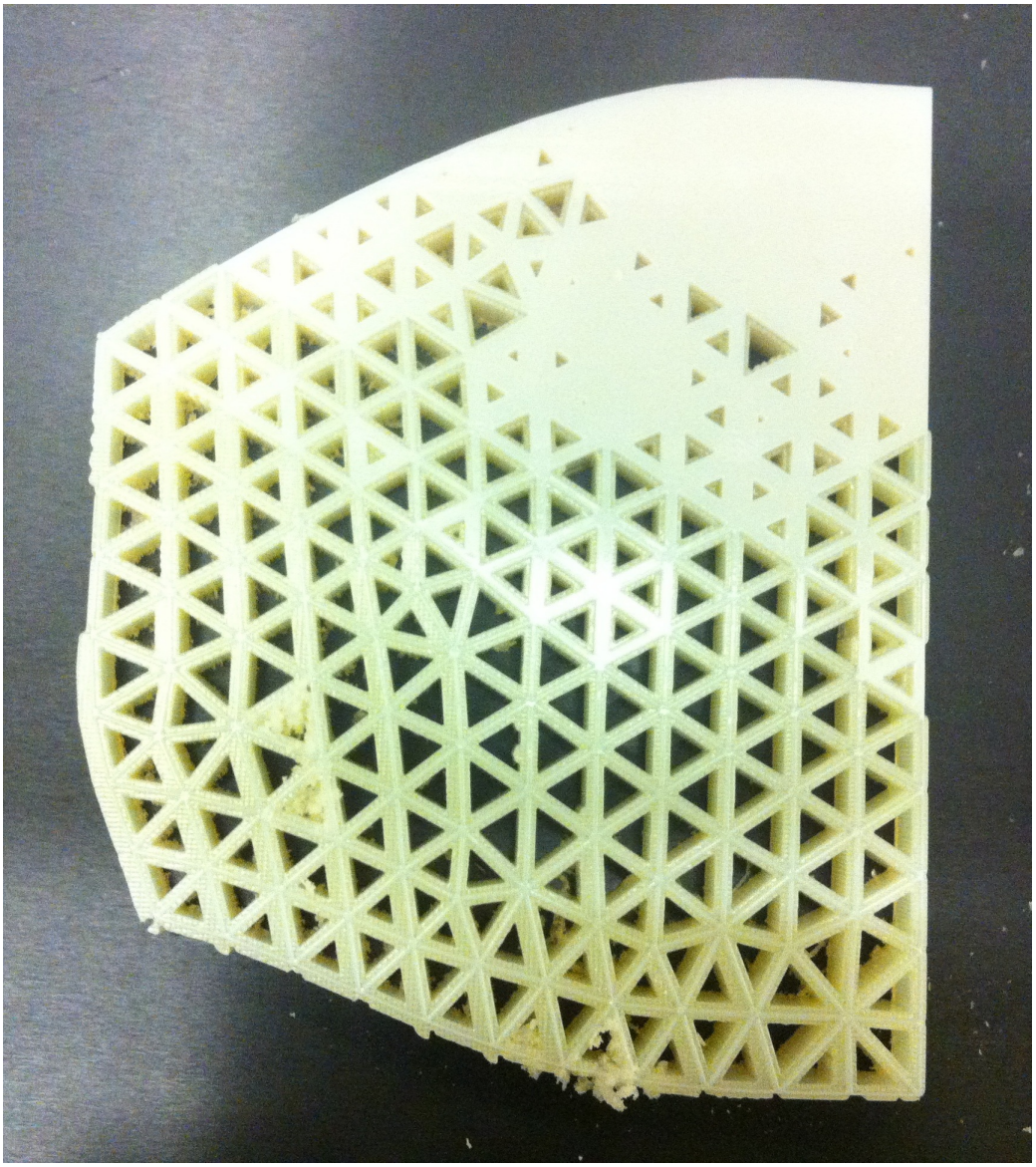

FIGURE 3.8. 3D printed lattice with support material

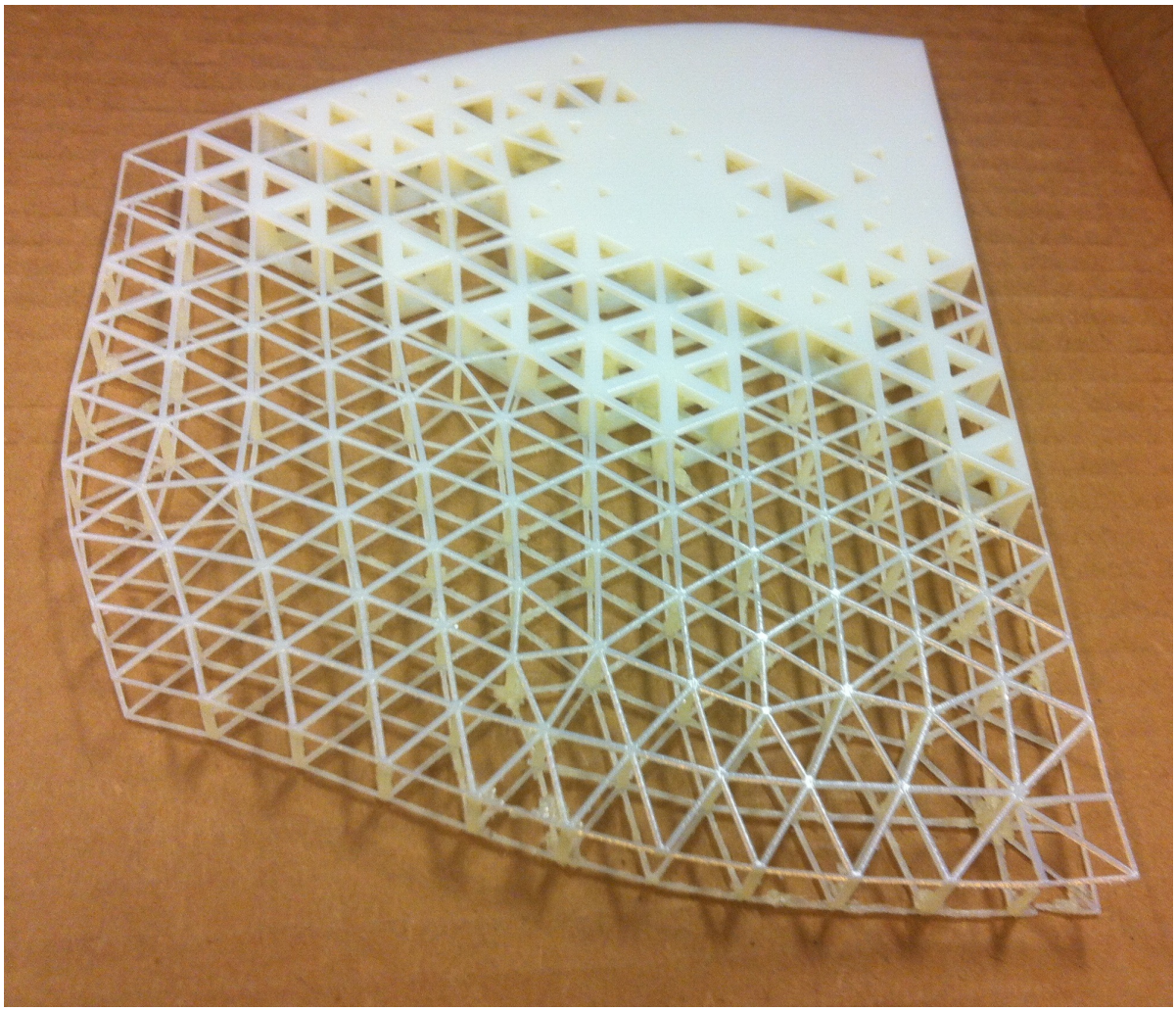

FIGURE 3.9. 3D printed clean lattice

CHAPTER 4

Discussion and Conclusions

4.1 Discussion

The research work reported in this thesis targeted the optimum design of a lattice structure for a bridge application. lattice materials belongs to an advanced class of material well known in the fields of biomedical engineering and aerospace. It has rarely been considered for architecture and construction applications. The theories involved for the study of lattice materials, mainly related to homogenization, applied through multi-scale analysis, were implemented by the author targeting an innovative bridge design. The design process incorporates an optimization procedure at the lattice microstructure level to produce optimum mechanical performance at the macro-scale.

The structural analysis results in Section 3.1, coupled with the Finite Element results in Section 3.2, demonstrate that the bridge structure with 11 ribs, of 1 m thickness each, supports the applied load. The same method incorporates both system and component scales as discussed in Sections 2.1 and 2.2. The procedure can be used to determine the appropriate number of ribs for different rib thicknesses, and compare the model obtained with the current design in terms of von Mises stress and internal loads.

The optimization results reported in Section 3.3 in the form of a Pareto front, show that the problem converged towards an optimum set of solutions, from which the designer can choose the one that best fits the design requirements. The convergence towards a plateau was monitored periodically during the iterations; it was observed that after 85 of the 100 iterations, approximately, convergence was reached.

The mapping results shown in Section 3.4 prove the capability of the selected method to map any relative density distribution for any type of geometry, whether in 2D or in 3D. So far, four element shapes were implemented, and lattices with either one or a combination of these elements can be produced. The method described in Section 2.4.2 can be extended to conduct the mapping process for other cell topologies, such as the octet truss, among many others. Hence, the bridge can be mapped with different unit cell topologies; the resulting structures can be compared in terms of their mechanical performance.

The manufacturing results in Section 3.5 show a sample of the lattice structure for a portion of the spine. As larger pieces can be built using the technology outlined in Section 2.5, a full prototype of the bridge can be constructed by assembling the different sections.

The contributions of this work are summarized below. First, the multi-scale approach detailed in Chapter 2 was applied to an innovative design of a bio-inspired pedestrian bridge. Second, the relative density distribution was translated to a geometrical model via a mapping procedure. Third, the feasibility of manufacturing a proof-of-concept prototype for parts of the bridge was demonstrated. Lastly, a brief discussion on the manufacturing materials and technologies for the natural-scale bridge was conducted.

4.2 Recommendations for Future Work

So far, the discussion has focused on the fabrication of a prototype of the bridge at a small scale using 3D printing; the subject of the construction of the bridge at the natural scale has not been addressed yet. This is the topic of this section. In terms of manufacturing processes, they can be categorized into two types: additive and subtractive. The opportunities of using each of them will be studied separately.

4.2.1 Additive Manufacturing. Lattice structures are conveniently fabricated with additive rather than subtractive manufacturing methods due to their highly porous nature. Building layer by layer using material deposition is far more efficient and economical than cutting holes through a large solid block, which can be not only material-wasting but also quite challenging to fulfill, considering the complexity of the unit cell interconnections, especially in lattices with gradient properties along the thickness and not only in-plane. In short, additive manufacturing (AM) is the most convenient with respect to process and cost. Nevertheless, the drawback is the constraint on the building volume of most, if not all, AM techniques. Here lies the task difficulty in relation to this particular project, since there is an established synergy between complex optimum microstructure and the design of large-scale structures. However, there are instances that prove that 3D printing is feasible at a large scale, if not immediately, in the foreseeable future. Some of these instances of AM technology are discussed here.

A Laser Melting Deposition (LMD) technique was developed in Beihang University (BUAA) by Professor Huaming Wang and his group, for the production of large aerospace components of titanium alloy. After many attempts, from 1995 until now, a building volume of 4×3×2 m was reached. The technique shown in Fig. 4.1 consists in deposition of material layer-by-layer using metal powder to fabricate full density near-net-shape components. Due to its ability of producing large complex parts, LMD

is quite attractive to the aerospace industry (Wang et al., 2012). Two large frames for aircraft components built with this process are displayed in Fig. 4.2 and 4.3.

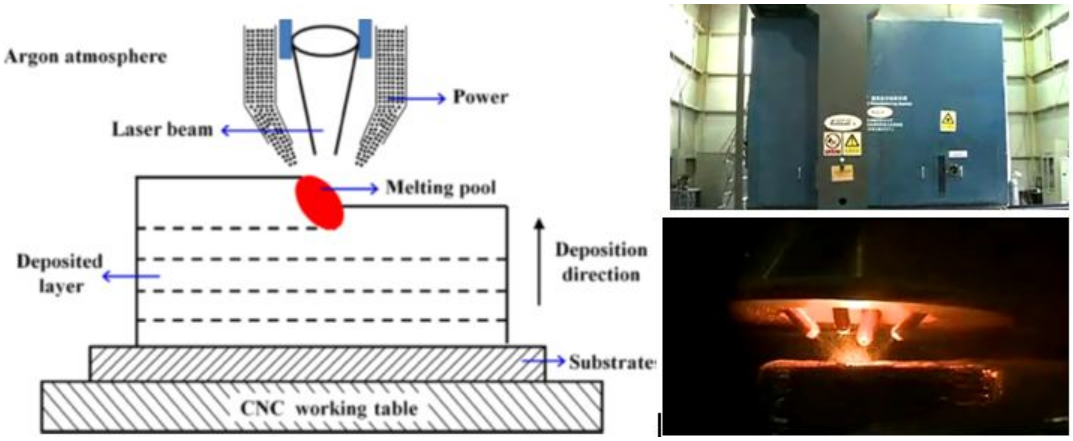

FIGURE 4.1. LMD system

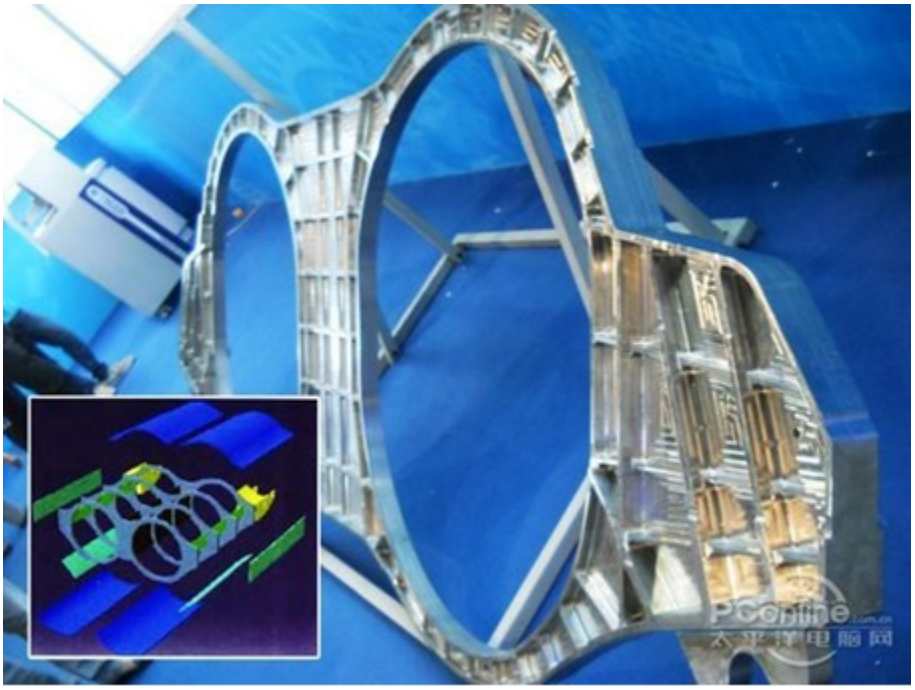

FIGURE 4.2. Large Integral Titanium Alloy Frame of Fighter Produced by LMD

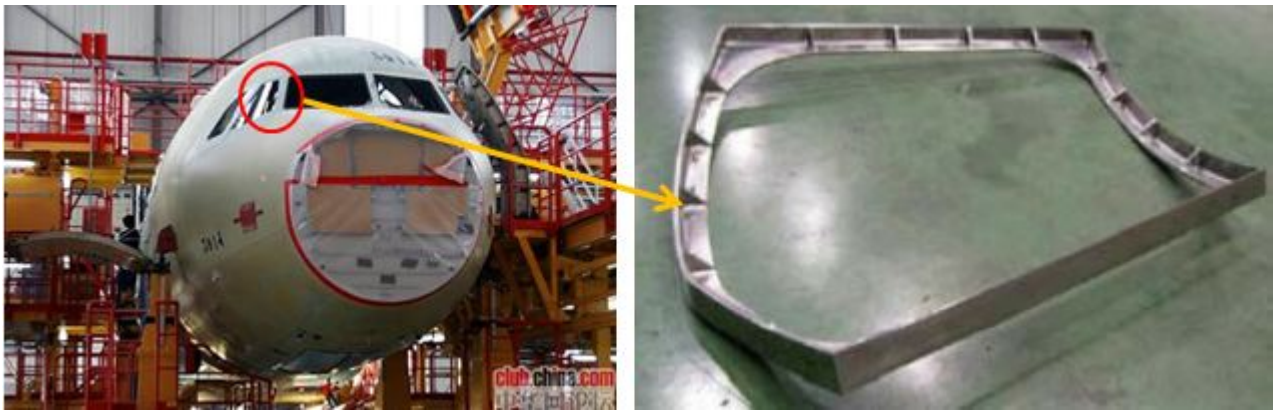

FIGURE 4.3. Window Frame

A large-scale production was attained with this LMD owing to the control of defects resulting from the drastic temperature drop that happens when the thermal source is moved away from the surface (Vrancken et al., 2012).

Another process is Direct Metal Laser Sintering (DMLS), developed in China's Northwestern Polytechnical University (NPU) by Professor Weidong Huang and his team. This technique, illustrated in Fig. 4.4, is highly appealing for the manufacturing of lattice material. It can build parts more than 5 m long, such as the aircraft section of Fig. 4.5.

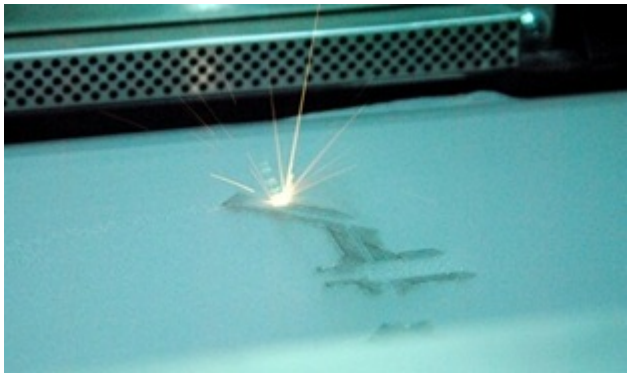

FIGURE 4.4. Direct Metal Laser Sintering

Enrico Dini, an Italian inventor, known as "The man who prints houses", has a passion for printing. He dreamt of building with concrete at large scale using an

FIGURE 4.5. Aircraft section more than 5 m high

innovative technique that does not require scaffolding and manpower. For that, he built in 2004 a 3D real scale printing machine that binds sand with epoxy. In 2007, he substituted epoxy with an inorganic binding material that is deposited through the nozzle right after the sand without using water. His real-scale 3D printer, which he called the D-shape, is illustrated in Fig. 4.6 (Lopez, 2011). Its building volume is 6×6×1 m, which enables the production of large components such as the one displayed in Fig. 4.7 (Mings, 2010). In terms of mechanical properties, the strength of the part obtained is comparable to reinforced concrete. As for cost, the overall building cost would be lower than traditional construction methods, since substantial savings happen in terms of scaffold and manpower, although the printing material is more

expensive than regular concrete. Figure 4.8 shows another cellular-like architecture manufactured by the D-shape.

FIGURE 4.6. The D-shape 3D printer by Enrico Dini

To make a long story short, additive manufacturing at the large scale is not a dream any more. With the advance of technologies around the world, AM seems to become more realistic with time. Taking a look at the techniques described above, one can be optimistic about the future of construction with AM, allowing the fabrication of a natural-scale pedestrian bridge, with a design similar to that of the bridge under discussion.

4.2.2 Subtractive Manufacturing. While additive manufacturing is in general more favourable for lattice structures, subtractive manufacturing remains a potential option, assuming the correct technology is available.

As previously mentioned, the complexity of the lattice structure is the crucial challenge for conventional machining processes. Moreover, these processes would

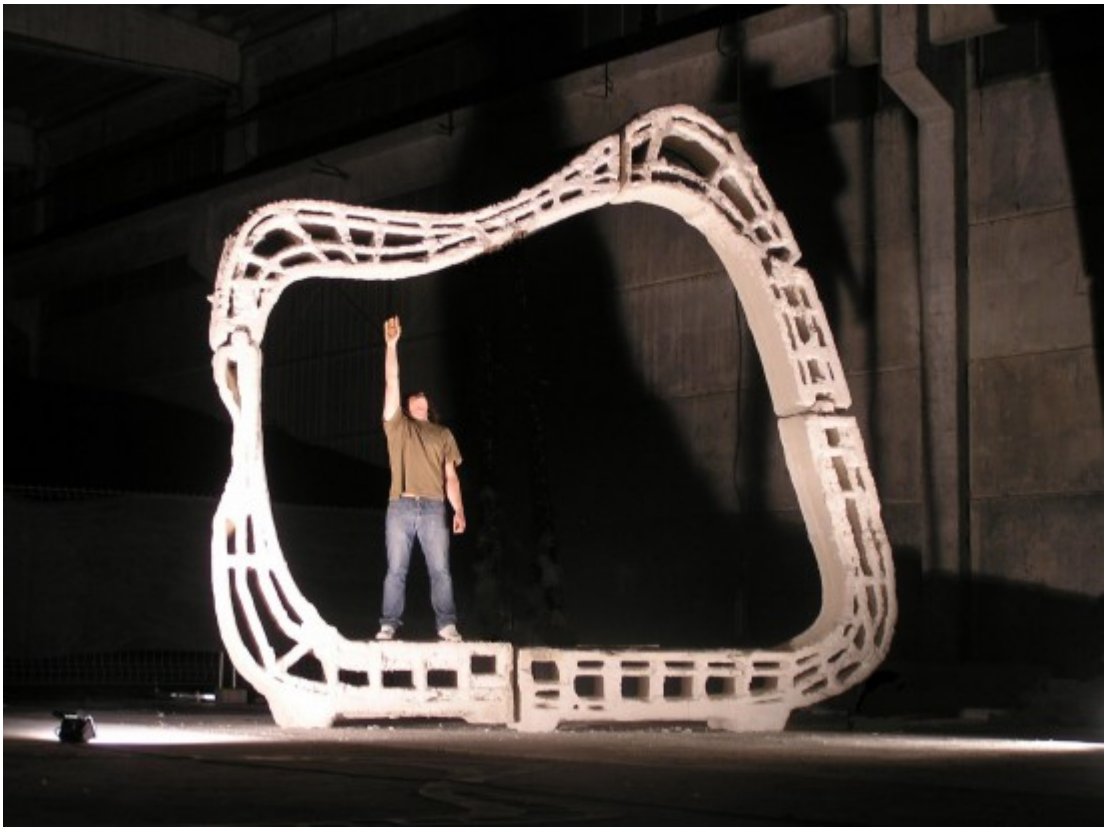

FIGURE 4.7. Small section of a room built by Enrico Dini for the Villa Rocce Project in Sardinia

also waste a substantial quantity of material because of the porous character of the lattice. Consequently, a smart powerful machining system is essential to build such an architecture. In that field, the six-axis FANUC robot is a leading candidate, knowing that it has been tested for homologous purposes at LIPHE. A picture of the robot is displayed in Fig. 4.9 with a close-up on the machining tool in Fig. 4.10. A lattice structure, shown in Fig. 4.11, having a square-cell topology and made of wood, was constructed using this technique. This demonstrates the feasibility of building components with lattice material using this robot. In fact, the machining tool has a length ranging from 100 to 300 mm and a diameter of 3, 6 or 12 mm. These values would set the limit on the smallest unit cell size that can be achieved with this technology. As for the dimensions at the macro-scale, the workspace of the

FIGURE 4.8. Enrico Dini working on the D-shape with a printed piece behind him

robot is displayed in Fig. 4.12. A maximum reach of 2.05 m can be attained with this robot, which allows fabrication of parts within that order of magnitude (FANUC, 2014). Therefore, the bridge can be divided into different modules that can be built separately and then assembled.

The work reported in this thesis can be extended in the future to incorporate more advanced features. For instance, in addition to optimizing the relative density distribution in the plane of the cross-section, it can also be optimized in 3D to obtain the optimal gradient properties also in the direction along the span of the bridge perpendicular to the cross-sectional plane. Furthermore, the rib thickness can be included as a design variable in the optimization procedure and, on the other hand,

FIGURE 4.9. Fanuc robot at LIPHE

the optimal shape of the ribs can be determined through topology optimization.

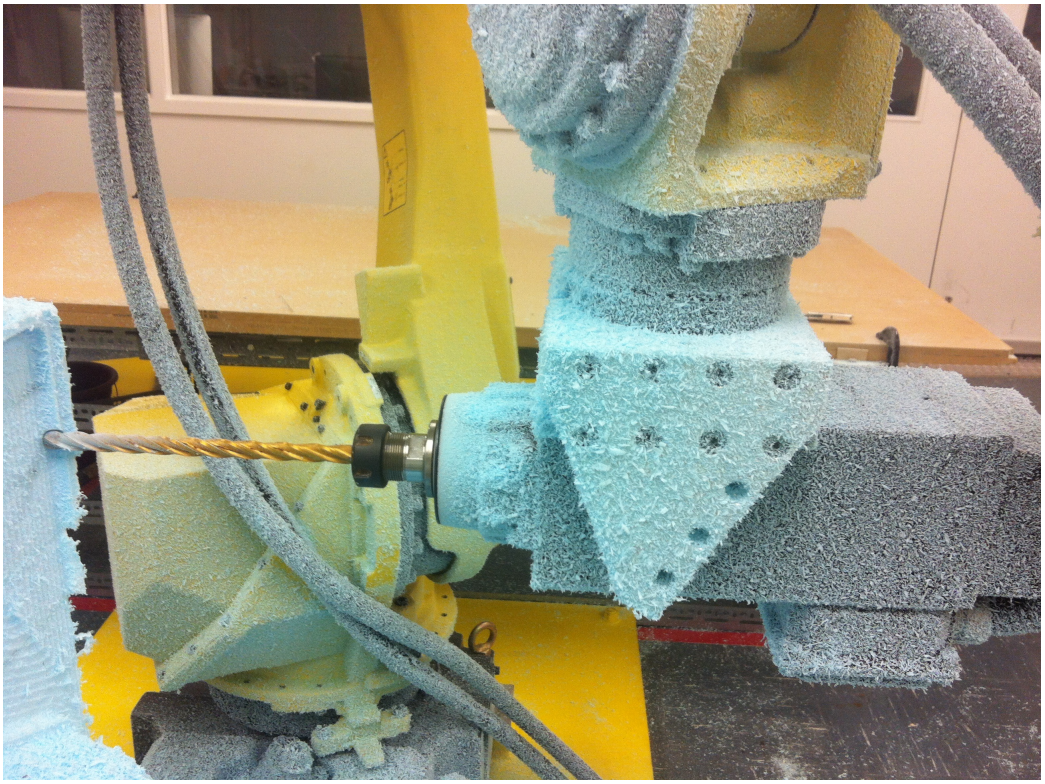

FIGURE 4.10. Machine tool of the Fanuc robot at LIPHE

Finally, the construction of the natural-scale bridge can be investigated to a greater extent and tested with available technologies.

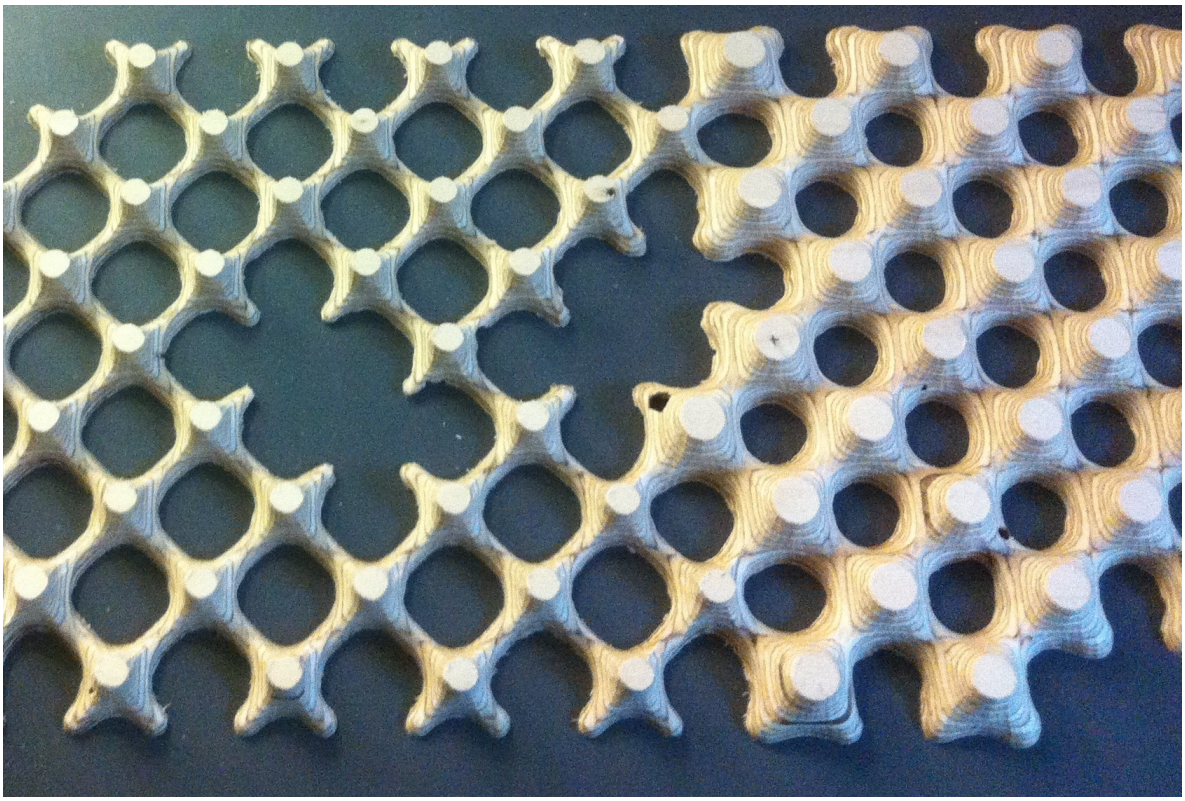

FIGURE 4.11. Wooden lattice built with subtractive manufacturing

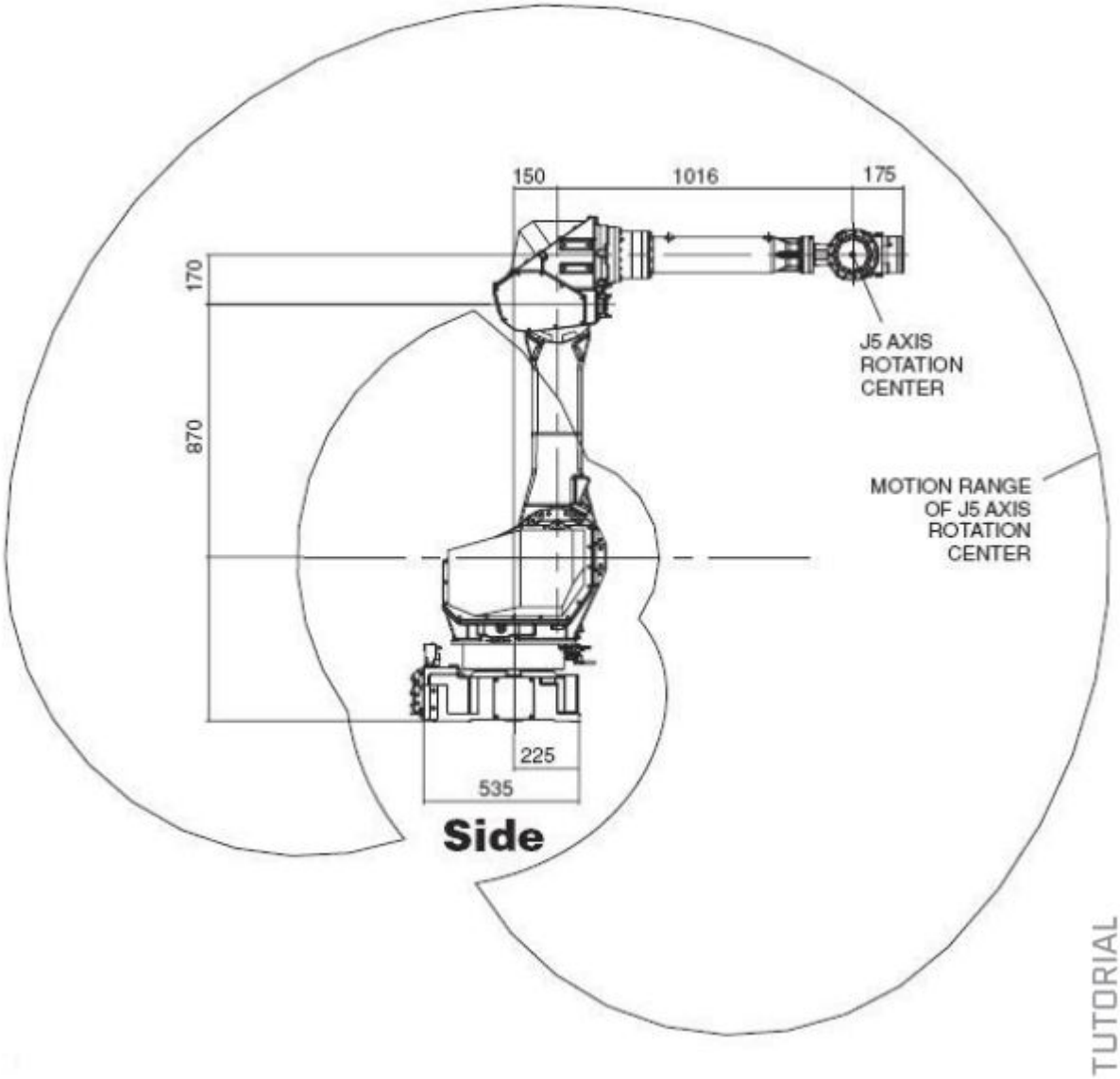

FIGURE 4.12. Workspace of the FANUC robot

BIBLIOGRAPHY

American Association of State Highway and Transportation Officials, "Load and Resistance Factor Design Guide Specifications for the design of pedestrian bridges", Second Edition, AASHTO (2009)

American Association of State Highway and Transportation Officials, "LRFD, Bridge Design Practice", AASHTO (2012)

Angeles J., "The Role of Entropy in Design Theory and Methodology", Lecture Notes of MECH593 Design Theory and Methodology, McGill University, Winter term (2007)

Anthoine A., "Second-order homogenization of functionally graded materials", International Journal of Solids and Structures 47 14771489 (2010)

Arabnejad S., Pasini D., "Mechanical properties of lattice materials via asymptotic homogenization and comparison with alternative homogenization methods", International Journal of Mechanical Sciences 77 249-262 (2013)

Arabnejad S., Pasini D., "Multiscale Design and Multiobjective Optimization of Orthopaedic Hip Implants with Functionally Graded Cellular Material", Journal of Biomechanical Engineering, vol 134 (3) (2012)

Beaulieu D., Picard A., Tremblay R., Grondin G. and Massicotte B.,"Calcul des charpentes d'acier", Institut canadien de la construction en acier (2003)

Benyus J.M., "Biomimicry: Innovation inspired by nature", William Morrow and company, New York (1997)

Berger J.R., Karageorghis A., "The method of fundamental solutions for heat conduction in layered materials", International Journal for Numerical Methods in Engineering, 45 pp. 16811694 (1999)

Canadian comission on building and fire codes,"Public Review on Proposed Changes to the 2010 National Model Construction" (2010)

Canadian Standrads Assosciation,"Canadian Highway Bridge Design Code", CAN/CSA-S6-06 (2006)

Cavalcante M., Marques S.,Pindera M.J., "Computational aspects of the parametric finite-volume theory for functionally graded materials", Computational Materials Science 44 422438 (2008)

Chopra P., "Effective mechanical properties of lattice materials", University of British Colombia (2011)

Chua, C.K., "Selective laser sintering of functionally graded tissue scaffolds", MRS Bulletin, v 36, n 12, p 1006-1014 (2011)

Deb K., "A Fast and Elitist Multiobjective Genetic Algorithm: NSGA-II", IEEE Transactions on evolutionary computations, VOL. 6, NO. 2 (2002)

Elsayed M., Pasini D., "Analysis of the elastostatic specific stiffness of 2D stretching-dominated lattice materials", Mechanics of Materials 42 709-725 (2010)

Elsayed M., Pasini D., "Multiscale structural design of columns made of regular octet-truss lattice material", International Journal of Solids and Structures 47 17641774(2010)

FANUC America Corporation, "Medium Payload Intelligent Robot, FANUC Robot M-710ic/50,/70", Accessed 04 Apr 2014. http://www.fanucamerica.com/products/robots/robotseries=M-710iC

Federal Highway Administration,"Serviceability limits and economical steel bridge design", US Department of transportation (2011)

Fish J., Belyteschko T., "A First Course in Finite Elements", John Wiley & Sons, Ltd (2007)

Fonseca C. M., Fleming P. J., "Genetic algorithms for multiobjective optimization: formulation, discussion, and generalization", pages 416423. The Fifth International Conference on Genetic Algorithms (1993)

French MJ., "Conceptual Design for Engineers", Springer (1999)

Gibson L.J. and Ashby M.F., "Cellular Solids, Structure and properties", Second edition, Cambridge Solid State Science Series (1997)

Goldberg D. E., Deb K.," A comparison of selection schemes used in genetic algorithms", Foundation of genetic algorithms, G.J.E. Rawlins (Ed.), pages 69-93 (1991)

Goldberg D. E., " Genetic Algorithms in Search, Optimization and Machine Learning, Reading", Addison-Wesley (1989)

Hassani B., Hinton E., "A review of homogenization and topology optimization I– homogenization theory for media with periodic structure", Computers & Structures, 69 707-717 (1998)

Hensel M., Menges A., Weinstock M.,"Emergence: Morphogenetic Design Strategies", Architectural Design, AD Magazine, Wiley-Academy (2004)

Hollister S.J. and Kikuchi N., "A comparison of homogenization and standard mechanics analyses for periodic porous composites", Computational Mechanics 10, 73-95 (1992)

Horn J., Nafplotis N., Goldberg D. E., "A niched pareto genetic algorithm for multiobjective optimization", pages 8287, Orlando. The First IEEE Conference on Evolutionary Computation, Piscataway: IEEE Neural Networks Council (1994)

Khoda, A.K.M., "A functionally gradient variational porosity architecture for hollowed scaffolds fabrication", Biofabrication, v 3, n 3, p 034106 (15 pp.) (2011)

Kieback B., Neubrand A., Riedel H., "Processing techniques for functionally graded materials", Materials Science and Engineering A362 81105 (2003)

Knowles J., Corne D., " The Pareto archived evolution strategy: A new baseline algorithm for multiobjective optimization", inProceedings of the 1999 Congress on Evolutionary Computation. Piscataway, NJ: IEEE Press, pp. 98105 (1999)

Liu T., Wang Q., Ao Gao, Zhang C., Wang C., He J., "Fabrication of functionally graded materials by a semi-solid forming process under magnetic field gradients", Scripta Materialia 57 992995 (2007)

Lopez O., "Manifestations: The Immediate Future of 3D Printing Buildings and Materials Science", 12 Nov 2011. ArchDaily. Accessed 04 Apr 2014. http://www.archdaily.com/?p=179148

Marin L.,Lesnic D., "The method of fundamental solutions for nonlinear functionally graded materials", International Journal of Solids and Structures 44 68786890 (2007)

Ming C. Leu, Bradley K. Deuser, Lie Tang, Robert G. Landers, Gregory E. Hilmas, Jeremy L. Watts, "Freeze-form extrusion fabrication of functionally graded materials", CIRP Annals - Manufacturing Technology 61 223226 (2012)

Mings J., "How big is the biggest 3D freeform architechture print? This big.", 05 May 2010. Accessed 04 Apr 2014. http://www.solidsmack.com/fabrication/enrico-dini-big-freeform-architecture-3d-print-sardinia-villa-rocce/

Otto F. and Rasch B., "Finding Form:towards an architecture of the minimal", Axel Menges (1995)

Pahl G. and Beitz W., "Engineering Design: A Systematic Approach", 2nd Edi- tion, Wallace, K.M. (editor); Blessing, L., Bauert, F. and Wallace, K.M. (translators),

Springer-Verlag, London (1996)

Pompea W., Worch H., Epple M., Friess W., Gelinsky M., Greil P., Hempele U., Scharnweber D., Schulte K., "Functionally graded materials for biomedical applications", Materials Science and Engineering A362 4060 (2003)

Rasheedat M. Mahamood, Esther T. Akinlabi Member, IAENG, Mukul Shukla and Sisa Pityana, "Functionally Graded Material: An Overview", Proceedings of the World Congress on Engineering 2012 Vol III, WCE 2012, July 4 - 6, London, U.K. (2012)

Schaffer J. D.," Multiple objective optimization with vector evaluated genetic algorithms", The First International Conference on Genetic Algorithms and their Applications, Hillsdale: Lawrence Erlbaum Associates, pages 93100, Pittsburgh, USA (1985)

Srinivas N., and Deb K., "Multiobjective optimization using nondominated sorting in genetic algorithms", Evolutionary Computation, 2:221248 (1995)

Tripathi V., Chauhan H., "Multi objective optimization of planetary gear train", Springer-Verlag Berlin Heidelberg editor, SEAL 2010, LNCS 6457, volume 350, pages 578582 (2010)

Tzonis A., "Santiago Calatrava: The poetics of movement", Universe Architecture Series, Universe (1999)

Vemaganti K.,Deshmukh P., "An adaptive globallocal approach to modelling functionally graded materials", Comput. Methods Appl. Mech. Engrg. 195 42304243 (2006)

Vigliotti A., Pasini D., "Stiffness and strength of tridimensional periodic lattices", Comput. Methods Appl. Mech. Engrg. 229-232 (2012)

Vrancken B., Thijs L., Kruth J.P., Humbeeck J.V., "Heat treatment of Ti6Al4V produced by Selective Laser Melting: Microstructure and mechanical properties",

Journal of Alloys and Compounds, 541(0): p. 177-185 (2012)

Wang Z., Guan K., Gao M., Li X., Chen X., Zeng X., "The microstructure and mechanical properties of deposited-IN718 by selective laser melting", Journal of Alloys and Compounds, 513(0): p. 518-523 (2012)

Wang A.-J., MDowell D.L., "In-plane stiffness and yield strength of periodic metal honeycombs", Journal of Engineering Materials and Technology, Vol.126 (2004)

Weinstock M., "The architecture of emergence: The evolution of form in nature and civilisation", John Wiley & Sons Ltd (2010)

Xia Qi,Yu Wang M., "Simultaneous optimization of the material properties and the topology of functionally graded structures", Computer-Aided Design 40 660675 (2008)

Zhang G., Guoa Q., Wang K., Zhang H., Songa Y., Shi J., Liu L., "Finite element design of SiC/C functionally graded materials for ablation resistance application", Materials Science and Engineering A 488 4549 (2008)

Zitzler E., " Evolutionary algorithms for multiobjective optimization: Methods and applications", Doctoral dissertation ETH 13398, Swiss Federal Institute of Technology (ETH), Zurich, Switzerland (1999)

Document Log:

Manuscript Version 0

Typeset by $\mathcal{AMS}$-LaTeX — 13 August 2014

Angela Badrieh

E-mail address: angelab@cim.mcgill.ca

Typeset by $\mathcal{AMS}$-LaTeX